

An Archival *Chandra* and *XMM-Newton* Survey of Type 2 Quasars

Jianjun Jia¹, Andrew Ptak², Timothy Heckman¹, Nadia L. Zakamska¹

¹*Department of Physics and Astronomy, Johns Hopkins University, Baltimore, MD 21218, USA*

²*Goddard Space Flight Center, Greenbelt, MD 20771, USA*

ABSTRACT

In order to investigate obscuration in high-luminosity type 2 AGN, we analyzed the *Chandra* and *XMM-Newton* archival observations for 72 type 2 quasars at $z < 1$. These objects were selected by cross-correlating the largest catalog of optically identified type 2 quasars to date selected from Sloan Digital Sky Survey (SDSS) with the *Chandra* and *XMM-Newton* archives. The type 2 quasar sample was selected based on the [O III] λ 5007 optical emission line which we assume to be an approximate indicator of the intrinsic AGN luminosity. The archival X-ray spectra were fitted with absorbed power-law models to characterize the spectral properties of each source. For 54 objects with good spectral fits, the observed hard X-ray luminosity ranges from 2×10^{41} to 5.3×10^{44} erg s⁻¹, with the median of 1.1×10^{43} erg s⁻¹. We find that the means of the column density and photon index of our sample are $\log N_{\text{H}} = 23.0$ cm⁻² and $\Gamma = 1.87$ respectively, which are consistent with results from deep X-ray surveys. The observed ratios of hard X-ray and [O III] line luminosities imply that the majority of our sample suffer significant amounts of obscuration in the hard X-ray band. We also fit the spectra using a more physically realistic model which accounts for both Compton scattering and a potential partial covering of the central X-ray source to estimate the true absorbing column density and use simulations to reproduce the observed $L_{\text{X}}/L_{[\text{O III}]}$ ratios. We find that the absorbing column density estimates based on simple power-law models significantly underestimate the actual absorption in approximately half of the sources. Eleven sources show a prominent Fe K α emission line, and we detect this line in the other sources through a joint fit (spectral stacking). The correlation between the Fe K α and [O III] fluxes and the inverse correlation of the equivalent width of Fe K α line with the ratio of hard X-ray and [O III] fluxes is consistent with previous results for lower luminosity Seyfert 2 galaxies. We conclude that obscuration is the cause of the weak hard X-ray emission rather than intrinsically low X-ray luminosities. We find that about half of the population of optically-selected type 2 quasars are likely to be Compton-thick. We also find no evidence that the amount of X-ray obscuration depends

on the AGN luminosity (over a range of more than three orders-of-magnitude in luminosity).

Subject headings: galaxies: active — quasars: general — X-rays

1. Introduction

In the standard unification model, all active galactic nuclei (AGN) are powered by accretion onto supermassive black holes (SMBHs), with different geometries resulting in various types of AGNs (Antonucci 1993). That is, AGN are grossly classified by whether broad emission lines are (type 1) or are not (type 2) present in the optical and UV spectrum. In the unified model, the central accretion disk and surrounding retinue of high velocity gas is directly visible in type 1 AGN, while this region is blocked from a direct view by a toroidal obscuring structure in type 2 AGN. In the local universe, low-luminosity type 2 AGNs (type 2 Seyfert galaxies) are found to be as abundant as type 1 AGNs (type 1 Seyfert galaxies), and the applicability of the unified model is well-established (Hao et al. 2005). Given the strong cosmic evolution of the AGN population, the most luminous AGN are very rare in the local universe and this population is only well-characterized at high redshift. Unfortunately, the heavy obscuration by the dense gas and dust surrounding the SMBH makes type 2 AGNs much fainter than type 1 AGN and they become difficult to discover at high redshifts. Thus, it is therefore unclear how well the standard unified model works for AGN of the highest luminosities and at high redshifts.

Indeed, X-ray surveys have shown that the ratio of type 2 to type 1 AGN decreases with AGN X-ray luminosity (Ueda et al. 2003; Sazonov & Revnivtsev 2004; Barger et al. 2005; Treister & Urry 2005; Akylas et al. 2006; Gilli et al. 2007; Fiore et al. 2008; Treister et al. 2008). For a review see Treister & Urry (2011). This is in contrast to the results from the infrared, radio and optical surveys (Reyes et al. 2008, see Lawrence & Elvis 2010 for review), which suggest that obscured AGNs are about as common as the unobscured ones at the highest probed luminosity.

In this paper we will explore the hard X-ray and optical emission-line properties of the largest *optically selected* sample available to date of highly luminous type 2 AGN. We will then compare these properties to those of typical low-luminosity AGN to test the unified model at high luminosity. We note that throughout the rest of our paper, we will use the term ‘Seyfert’ to refer to low-luminosity AGN, and ‘quasar’ to refer to high-luminosity AGN (with a dividing line at a bolometric luminosity greater than 10^{45} ergs s^{-1}).

A large sample of type 2 quasars are needed in order to test how and if the unified model

applies at high luminosities. Although the central AGN is hidden from view in type 2 AGN, the strong UV radiation escaping along the polar axis of the obscuring material distribution photo-ionizes circum-nuclear gas leading to strong narrow high-ionization emission-lines. Since this narrow-line region is at larger radii than the bulk of the obscuring material, selection based on narrow optical emission lines promises to be less biased against type 2 AGN than hard ($E < 10$ keV) X-ray surveys (see, e.g., LaMassa et al. 2009, 2010). Since the narrow line emission mechanism is the same for both type 1s and 2s in the standard AGN model, we can expect that the line luminosity serves as an indicator of the intrinsic luminosity of the nucleus, and when compared with the observed hard X-ray luminosity, as a diagnostic of X-ray obscuration.

Zakamska et al. (2003, hereafter Z03) selected 291 type 2 quasars at redshifts $0.3 < z < 0.83$ based on their optical emission line properties from the spectroscopic data of the Sloan Digital Sky Survey (SDSS; York et al. 2000). They found strong narrow emission lines with high-ionization line ratios but no broad emission lines in these objects, and therefore identified them as type 2 quasar candidates based on [OIII] $\lambda 5007$ emission-line luminosities greater than $10^8 L_{\odot}$. This new method has greatly expanded the number of type 2 quasars known, and it allows the properties of type 2 quasars to be studied in detail. Subsequent multi-wavelength studies (Zakamska et al. 2004, 2005, 2006; Ptak et al. 2006; Vignali et al. 2006) confirmed that the standard models for AGNs could give good descriptions of those optically selected type 2 quasars. Vignali et al. (2010, hereafter V10) recently studied the X-ray spectra of 25 type 2 quasars from Zakamska et al. (2003), by comparing the measured hard X-ray luminosity with the intrinsic (de-absorbed) X-ray luminosity derived from the [O III] $\lambda 5007\text{\AA}$ and mid-IR ($5.8\mu\text{m}$ and $12.3\mu\text{m}$) line estimators, and concluded that about half of the SDSS type 2 quasars with exceptionally high luminosities ($L_{[\text{O III}]> 10^{9.3} L_{\odot}$) might be Compton-thick (absorbing column density $N_{\text{H}} > 10^{24} \text{cm}^{-2}$).

By applying the same selection technique to the more recent data, a catalog containing 887 type 2 quasars from SDSS was released by Reyes et al. (2008, hereafter R08), which expanded the original sample by a factor of four, preferentially at higher [O III] luminosities. We selected the objects covered in X-ray archival observations from this pool, and investigated their X-ray properties. These objects provide the largest sample of X-ray type 2 quasars which have no bias with respect to X-ray luminosity, since they are selected on the basis of optical line emission. In this paper, we present our study of 72 type 2 quasars observed by *Chandra* and *XMM-Newton*. Section 2 describes our sample selection and data analysis. Section 3 gives the X-ray spectral analysis. We discuss our results in Section 4 and come to conclusions in Section 5. An $h = 0.7$, $\Omega_m = 0.3$ and $\Omega_{\Lambda} = 0.7$ cosmology is assumed throughout this paper (Spergel et al. 2003).

2. Sample Description and Data Analysis

By correlating those 887 optically selected type 2 quasars with the public *Chandra* (within a 5′ search radius) and *XMM-Newton* (within a 15′ search radius) archives, 72 quasars were found to be covered by *Chandra* or *XMM-Newton* or both as of February 2011¹. The list of the coordinates, Galactic column density, redshift, [O III]λ5007Å luminosity, observation ID, exposure time, observation date and off-axis angle for each target is given in Table 1, where objects are identified by their J2000 coordinates and shortened to *hhmm+ddmm* notation elsewhere. Some sources were also studied and published in other papers, and they are marked in the last column of Table 1.

The data pipeline is done by **XAssist**², which is a software package for automatic analysis of X-ray astrophysics data. Point sources with sufficient photons are detected by **XAssist** automatically. However, in cases where sources are not detected due to insufficient counts, user-specified region files which contain the source coordinates are supplied as input to **XAssist**. CIAO (ver. 4.3) and XMMSAS (ver. 10.0.0) were called in processing *Chandra* and *XMM-Newton* data, respectively. The size of each point source extraction region is set by fitting an elliptical Gaussian function to a “stamp” image for each source, which typically results in a region size of 2″ (*Chandra*) and 18″ (*XMM-Newton*) for on-axis sources. Depending on how large the off-axis angles are, the region sizes of *Chandra* sources vary from about 4″ to 9″, and those of *XMM-Newton* sources vary from about 20″ to 40″. Background regions are set as annuli centered on the sources, but if the source is located in a crowded region or on the edge of the detector, another circular region in the field was chosen manually for background extraction.

3. Spectral analysis

We extract the spectra in the energy range of 0.3-10 keV for the *XMM* observations, and 0.3-8 keV for the *Chandra* ones. X-ray spectral fitting is performed with **XSPEC** (ver. 12). The spectra are grouped to one count per bin, and the *C*-statistic (Cash 1979) is used in fitting the spectra. Although the *C*-statistic is devised for unbinned spectra, *C*-statistic fitting in **XSPEC** performs better if the spectra are binned to at least one count per bin (Teng et al. 2005). For those sources with more than 200 photon counts collected, we

¹This work was performed using the High-Energy Astrophysics Science Archive (HEASARC), <http://heasarc.gsfc.nasa.gov>

²version 0.9993, <http://xassist.pha.jhu.edu>

group their spectra to 10 counts per bin, and use χ^2 statistic in the spectral fitting. X-ray photons are collected by three detectors on *XMM-Newton* i.e., PN, MOS1 and MOS2. The two MOS spectra are combined and fitted simultaneously with PN spectra in **XSPEC**, and all parameters are tied together except for a constant multiplicative factor to account for relative flux calibration differences among the detectors. Five *XMM-Newton* sources have counts detected in only one or two of the three detectors, which are noted in the second column in Table 2. Errors are calculated at 90% significance, i.e., $\Delta\chi^2$ or $\Delta C = 2.7$ for one interesting parameter.

The X-ray spectra of obscured (type 2) AGN can be complex (see Turner et al. 1997; Risaliti 2002; LaMassa et al. 2009), and no single model could fit the spectra well in all cases. Thus, we carry out the spectral fit with **XSPEC** using several spectral models:

(1) Single-absorber power-law: Initially, the spectrum is fitted as a power-law continuum absorbed by the Galactic column density ($N_{\text{H,G}}$) and an intrinsic redshifted absorption column density (N_{H}). This model results in three free parameters: the column density N_{H} , the photon index Γ , and the power-law normalization. The Galactic neutral hydrogen column density $N_{\text{H,G}}$ is a fixed parameter (Dickey & Lockman 1990), which is calculated from HEAsoft N_{H} tool. However, in some cases, we fixed the photon index at $\Gamma = 1.7$ (which is a typical value for AGN, Nandra et al. 2005) if it is unconstrained, i.e., the errors exceeded reasonable bounds. We list the photon counts, the column densities and the photon indices of the spectral fits in Table 2, as well as the derived observed and intrinsic 2-10 keV luminosities and the ratios of the X-ray to [O III] luminosity. Some quasars have very small column densities in the spectral fits, and we use the upper limit instead in Table 2. The spectral plots of each quasar are shown in Figure 1.

There are 16 objects observed by *Chandra* having fewer than 10 photon counts, and 2 objects observed by *XMM* with detected total photon numbers fewer than the estimated mean background counts. The photon counts are too low to constrain the spectral parameters in spectral fitting. Therefore, we calculate the upper limit of the 2-10 keV flux at a $3\text{-}\sigma$ level. We assume that their spectra are an absorbed power-law with $\Gamma = 1.7$ and $N_{\text{H}} = 10^{23} \text{ cm}^{-2}$, which is a mean value of the column densities given in Table 2. The $3\text{-}\sigma$ upper limit of the 2-10 keV photon count rates are calculated by using the Bayesian statistical method by Kraft et al. (1991). We determined the count rate to flux conversion coefficient using **XSPEC**, and multiply it by the count rate upper limit to calculate the 2-10 keV flux upper limit. The detected counts, the source count upper limits, and the associated upper limits of the count rates, fluxes and luminosities are listed in Table 3.

(2) Double-absorber power-law: In the case of partial covering or the case of some X-ray flux being scattered into the line of sight around a higher column density absorber, a single

absorbed power-law cannot model the data accurately (LaMassa et al. 2009). Thus, we add another absorbed power-law component to the spectral fits in 23 cases which either have more than 100 photon counts or show high data-to-model residuals in their single-absorber power-law fits. The photon indices of both power-law components are tied together when fitting the spectra. However, tying the photon indices in the case of SDSS J1034+6001 results in a very large χ^2 , and we thus use two different indices in fitting its spectrum.

Table 4 lists the parameters and luminosities from their double-absorber model fits, and their spectral plots are shown in Figure 2. As shown in Table 4 we find that χ^2 or C -stat for most of the targets is significantly reduced by adding the second absorber component. The calculated F -test and significance of adding an additional component are also given in Table 4. The column densities of the second absorber ($N_{\text{H},2}$) are about one order of magnitude larger than those from their single-absorber models.

(3) Absorbed power-law plus Gaussian Fe K α line: If there is a prominent Fe K α emission line by visual detection, a Gaussian component was added to the power-law continuum. We initially fixed the line energy E_{line} at 6.4 keV (in rest frame) and the line width (σ) at 0.01 keV ($\sim 10\%$ of the instrumental line resolution for *Chandra* and *XMM-Newton*). In **XSPEC**, we first **ignore** the photon counts in the energy range of 5-7 keV to get the power-law index of the continuum, and then **notice** them to fit the emission line around 6.4 keV. Eleven objects show visually-detected emission lines, and the Gaussian fit parameters as well as the equivalent width and line luminosity are listed in Table 5. We also list the change of χ^2 if we remove the Gaussian component from the spectral fit to show how significant this emission line is.

4. Results and discussions

4.1. Column density and photon index distribution

Of our 72 quasars, at least crude spectral fitting is possible for 54. For these, we find that the mean power-law index is $\Gamma = 1.63 \pm 0.80$, where the error bar is the standard deviation of the power-law indices of the sample neglecting the individual fitting errors. This value is based on the single-absorber power-law fit results in Table 2, and those with photon indices fixed at 1.7 are not included. In the case that there are multiple observations for one object, we use the values of the simultaneous joint fit instead. The mean value is consistent with the result of a sample of obscured AGNs selected by *INTEGRAL*, which finds the mean value of photon index is $\Gamma = 1.68$ but with a smaller standard deviation of $\sigma = 0.30$ (de Rosa et al. 2012). However, if we replace the photon indices of those objects having double-absorber

power-law fits with the values listed in Table 4 we find $\Gamma = 1.87 \pm 0.74$, which is slightly larger. If we use only the results in Table 4 for double-absorber power-law fits, it becomes even larger, i.e., $\Gamma = 2.14 \pm 0.62$. This distribution is much like the one found in the best fits of a sample of local Seyfert 2s studied by LaMassa et al. (2009), where more than half of the objects have double-absorbed power-laws as their best-fitting model. We show such comparison in Figure 3.

By excluding those with upper limits for their column densities in spectral fits, we find the mean N_{H} of our sample is $\log N_{\text{H}} = 23.0 \pm 0.9 \text{ cm}^{-2}$, whose distribution is consistent with those Seyfert 2s as shown in Figure 4. We will discuss the possible luminosity dependence of obscuration in the following sections.

4.2. The $L_{\text{X}}/L_{[\text{O III}]}$ ratio as an indicator of obscuration

As the $[\text{O III}]\lambda 5007$ line emission originates in the narrow line region and so is not affected by the circumnuclear obscuration, the ratio between the observed hard X-ray (2-10 keV) and $[\text{O III}]$ line luminosity could be used as an indicator of the obscuration of the hard X-ray emission (Heckman et al. 2005; LaMassa et al. 2009). We list the $L_{\text{X}}/L_{[\text{O III}]}$ ratios in Tables 2 and 4, where we use the luminosities from the double-absorber power-law fit when there are sufficient counts. In Figure 5, we plot a histogram of the $L_{\text{X}}/L_{[\text{O III}]}$ ratios for our sample. We also show the observed distributions for type 1 (dashed blue line) and type 2 AGN (dot-dashed red line) (Heckman et al. 2005). The X-ray to $[\text{O III}]$ luminosity ratio of our sample agrees well with that of type 2 AGNs from Heckman et al. (2005), indicating that this sample is also likely experiencing obscuration. However, the fitted obscuring column densities inferred from the single-absorber power-law spectral fits are often too low to be consistent with the $L_{\text{X}}/L_{[\text{O III}]}$ ratios of type 2 quasars, e.g., the single-absorber model likely underestimates the amount of X-ray obscuration in our sample. Thus, we estimate their obscuration in the following subsection by using the X-ray to $[\text{O III}]$ ratios.

4.3. Estimation of the absorbing column density

As mentioned above, the derived observed $L_{\text{X}}/L_{[\text{O III}]}$ ratio in Table 2 and 4 implies that the targets in our sample are more highly obscured than would be implied by the fitted column densities N_{H} from our spectral models, i.e., the column density is underestimated in our spectral fits for at least half of the whole sample. We therefore use the correlation between the hard X-ray and $[\text{O III}]$ luminosity for both type 1 and 2 AGNs (Heckman et al. 2005)

to more realistically estimate the absorbing column densities of our targets (LaMassa et al. 2009). We employ a Monte Carlo approach to take the dispersion in the Sy 1 $L_X/L_{[\text{O III}]}$ distributions into account. First we generate 1000 random numbers which follow a Gaussian distribution with the same mean and dispersion as the $L_{2-10 \text{ keV}}/L_{[\text{O III}]}$ distribution of unobscured (type 1) AGNs in Heckman et al. (2005). Simulated unobscured 2-10 keV X-ray luminosities are computed by multiplying these values by the observed $[\text{O III}]$ luminosities for each AGN. The difference between the predicted unobscured X-ray luminosity and the observed value is considered to be due to absorption. Secondly, we make a look-up table of predicted count rates and fluxes corresponding to the column densities varying from 0 to 10^{25} cm^{-2} for each target in XSPEC. The expected count rates and fluxes are computed based on a partial covering model with covering fraction of 0.99 and photon index fixed at 1.7. We then interpolate the effective column density $N_{\text{H, sim}}$ that predicts a model count rate consistent with the observed count rate using the look-up table.

We compare the results from these simulations and the single- and double-absorber power-law spectral fits in Figure 6. The fitted N_{H} values from the single-absorber model (black plus symbols) are systematically lower than the simulated column densities, while $N_{\text{H},2}$ from double-absorber model (red asterisks) are more consistent with the simulated column densities, showing that not surprisingly more complex spectral models do a better job of recovering the intrinsic column density implied by the attenuated X-ray flux relative to the $[\text{O III}]$ emission.

Additionally, we used the *plcabs* model in XSPEC (Yaqoob 1997) to fit the spectra in order to approximately take Compton scattering into account (this model assumes a spherical covering which is not likely to be the case). In our fitting, the number of scatterings is set equal to 1 for $0 < N_{\text{H, sim}} < 10^{24} \text{ cm}^{-2}$, 5 for $10^{24} < N_{\text{H, sim}} < 5 \times 10^{24} \text{ cm}^{-2}$, and 12 for $N_{\text{H, sim}} > 5 \times 10^{24} \text{ cm}^{-2}$. The results of simulated column densities from both partial covering model and *plcabs* are shown in Table 7, where the lower limits for the simulated N_{H} are derived according to the upper limits of the photon count rates in Table 3. As shown in Table 7 about half of the sources have a fitted column density $N_{\text{H, plcabs}}$ much lower than the simulated $N_{\text{H, sim}}$. This indicates that direct spectral fitting still underpredicts the column density even by introducing Compton scattering in some cases, which reaffirms the necessity of using $L_X/L_{[\text{O III}]}$ ratio as an indicator of intrinsic obscuration. In summary these results imply that high signal-to-noise broadband spectra fitted with more complex (and realistic) models are more likely to recover the true (higher) column densities than simple power-law fits. This is also seen in lower luminosity Seyfert 2 galaxies (LaMassa et al. 2009; Rigby et al. 2009; Melendez et al. 2009).

4.4. Iron Line Emission

A significant iron emission line is found in 11 of the type 2 quasars (see Table 5). For the rest of the sample which do not show a significant Fe $K\alpha$ component in their individual spectra, we grouped them according to their observed $L_X/L_{[\text{O III}]}$ ratio, and then applied a ‘spectral’ stacking procedure. In Table 6, we show the four bins of the X-ray to [O III] luminosity ratio that are used to group the sources (where again the $L_X/L_{[\text{O III}]}$ values are from Table 4 if double-absorber power-law fits are performed), and we exclude those with photon counts fewer than 10 in the 2-10 keV band. We load the spectra of the objects in the same bin into **XSPEC** and only fit their spectra in the 3-8 keV range to minimize the impact of the spectral complexity discussed above. We assume that they have approximately the same properties for the power-law continuum and iron emission line. The intrinsic line width (σ) in the Gaussian component is fixed at 0.01 keV (i.e., unresolved for CCD spectra), and the photon indices of the continuum power-law is fixed at 1.7. The spectrum of each object is not physically shifted to account for redshift since the redshift is instead taken into account in the spectral model. The normalization of the power-law component and the line energy parameter of the Gaussian component are tied together between the fits, but the overall normalization for each source is allowed to be free. The line energy and equivalent width of iron line of each bin are shown in Table 6.

We show the correlation between the (effective average) Fe $K\alpha$ equivalent width (EW) and the ratio of hard X-ray and [O III] luminosities ($L_X/L_{[\text{O III}]}$) in Figure 7. This includes the stacking procedure along with the 11 quasars with prominent iron lines in Table 5 (black plus symbols with error bar), the four groups classified by their $L_X/L_{[\text{O III}]}$ ratio in Table 6 (blue plus symbols without error bar), and the sample of type 2 Seyfert galaxies from LaMassa et al. (2009) (red asterisk with error bar). Two objects (SDSS J1218+4706 and SDSS J1238+0927) are included in both our sample and theirs, and we use the EW and luminosity in Table 5 to make the plots as both papers give similar results. In order to fit the correlation by taking the upper limits into account, we use survival analysis **ASURV** Rev 1.2, which implements the method presented in Isobe & Feigelson (1990) and Lavalley et al. (1992) to investigate the correlation between these two parameters (log EW in units of eV and $L_X/L_{[\text{O III}]}$), which uses the bivariate data algorithm by Isobe et al. (1986). The correlation coefficient found in the survival analysis is -0.52 ± 0.10 , and it is significant at the a level of $> 99\%$.

We also investigate the correlation between the iron emission line luminosity and the [O III] luminosity by applying survival analysis. This is shown in Figure 8, which includes the 11 individual objects listed in Table 5 (symbols in black), the sample from LaMassa et al. (2009) (symbols in red) and those in our sample with no visually-detected iron lines (symbols

in blue). For those not listed in Table 5, we grouped them in bins defined by their [O III] luminosities. The iron line luminosity in each bin is calculated as the mean of $L_{[\text{O III}]}$ by multiplying the ratio of $\langle f_{\text{Fe}} \rangle / \langle f_{[\text{O III}]} \rangle$, where $\langle f_{\text{Fe}} \rangle$ and $\langle f_{[\text{O III}]} \rangle$ are the means of iron line and [O III] fluxes in this bin respectively. The mean values of iron line luminosity in the bins of $L_{[\text{O III}]}$ are listed in Table 8, where the error of L_{Fe} is calculated using error propagation of δf_{Fe} and $\delta f_{[\text{O III}]}$. The slope of the linear regression fit is 1.31 ± 0.24 , compared with the value of 1 given by Ptak et al. (2003) and 0.7 ± 0.3 by LaMassa et al. (2009), implying that the Fe K α line luminosity is roughly tracking the intrinsic AGN luminosity in a similar fashion to lower luminosity obscured AGN.

4.5. Luminosity Dependence of Obscuration

LaMassa et al. (2011) studied a sample of 45 type 2 Seyfert galaxies selected based on their mid-infrared continuum and [OIII] λ 5007 and emission line fluxes. They found that the observed hard X-ray to [O III] flux ratios are one order of magnitude lower on average than that of type 1 Seyfert galaxies (in agreement with Heckman et al. 2005), and they show a continuum of inferred X-ray obscuration without a clear separation into Compton-thin and Compton-thick populations. Here we similarly find that there is no strong break in the distributions of either the fitted N_{H} distribution or the $L_{\text{X}}/L_{[\text{O III}]}$ ratio for high luminosity type 2 AGN (Figure 4 and 5). We also find that the correlation between the Fe K α and [O III] luminosities is evidently the same between this sample of type 2 quasars and type 2 Seyfert galaxies. Finally, Figure 7 shows that the correlation between the EW of iron line and the $L_{\text{X}}/L_{[\text{O III}]}$ ratio is also the same for both the low luminosity (Seyfert) and high luminosity (quasar) type 2 AGN. Taken together, these results show that low and high luminosity optically- selected type 2 AGN luminosities have similar properties with respect to their X-ray obscuration.

We examine the possible luminosity dependence of obscuration more directly in Figure 9, in which we plot the column density of the second absorber versus the observed [O III] luminosity for those AGN having double- absorber power-law fits in Table 4. We also add the corresponding data for the type 2 Seyferts from LaMassa et al. (2009). There is no tendency for the column density to be correlated with the [O III] luminosity (over a range of more than three orders-of-magnitude in luminosity). Finally, in Figure 10 we plot the [OIII] luminosity vs. the hard X-ray luminosity for the combination of our type 2 quasar sample and the LaMassa et al. type 2 Seyfert sample. Using survival analysis to account for the objects with upper limits on the X-ray luminosity we find a best-fit slope in the log-log plot of 0.88 ± 0.11 (consistent with no significant luminosity-dependent X-ray obscu-

ration). In fact, type 1 AGNs show a systematic decrease in the ratio of hard X-ray to bolometric luminosity (e.g., Marconi et al. 2004). If the [OIII] luminosity is proportional to the bolometric luminosity, and if the amount of X-ray obscuration is independent of AGN luminosity, then the relationship in Marconi et al. (2004) would imply a slope of ~ 0.8 . This is fully consistent with the fitted slope in Figure 10. Recently, Jin et al. (2012) reported a nearly linear correlation between [O III] and $L_{2-10\text{keV}}$ of a sample of type 1 AGNs selected from the cross-correlation of the 2XMMi and SDSS DR7 catalogs. We show the correlation with the slope found by them in Figure 10 with 1σ deviation of our sample, where the line is shifted 1.26 dex downward to line up with the sample in this paper. This offset between the type 1 sample by Jin et al. (2012) and our type 2 sample is consistent with that reported by Heckman et al. (2005), indicating that L_X/L_{OIII} ratio is still a good indicator of intrinsic obscuration for high-luminosity AGNs.

Additionally, we compare the ratio of their X-ray and [O III] luminosity with their geometric means in Figure 11. There appears to be a slight correlation (slope 0.24 ± 0.09 in log-log scale) between the two quantities as shown in the upper panel of Figure 11. However, if we exclude those highly-obscured sources with $L_X/L_{\text{OIII}} < 1$, this correlation becomes negligible, i.e., the slope is nearly zero (see the lower panel of Figure 11). Comparing both cases, we find that the “correlation” in the left panel of L_X/L_{OIII} vs. $(L_X L_{\text{OIII}})^{1/2}$ is driven by the highly-obscured AGNs at lower luminosity.

4.6. The Fraction of Compton-thick AGN

In order to explain the X-ray background (XRB) spectrum above 10 keV, Gilli et al. (2007) predict that the population of Compton-thick AGN is as numerous as that of Compton-thin ones in their synthesis model of XRB fitting.

In Figure 12, we plot the column densities we derived from the simulations described in Section 4.3 versus the $L_X/L_{[\text{O III}]}$ ratio. Since N_{H} is derived from the difference between the typical Seyfert 1 $L_X/L_{[\text{O III}]}$ value and our observed $L_X/L_{[\text{O III}]}$, it is not surprising that we find that the $L_X/L_{[\text{O III}]}$ ratio decreases as the simulated N_{H} increases. We designate a source as a Compton-thick candidate if the 1σ confidence interval of simulated column density exceeds $1.6 \times 10^{24} \text{ cm}^{-2}$ in Figure 12. In addition, sources with an iron line EW larger than 1 keV in Table 5 are also considered to be Compton-thick. By also including the three sources which have no hard X-ray photons detected, we find 38 quasars out of 72 ($53 \pm 9\%$) are classified as Compton-thick. We flagged them in Table 2 and 3.

4.7. Sample completeness and selection bias

As stated above, in a sample of 25 obscured quasars optically selected from SDSS, V10 estimated the intrinsic X-ray luminosity from the observed [O III] emission line flux using Mulchaey et al. (1994), and compared it with the observed X-ray luminosities, i.e., similar to our simulation procedure although our simulations take the dispersion in the Seyfert 1 distribution into account. V10 conclude that a quasar could be identified as Compton-thick if the ratio between the observed and predicted X-ray luminosities is less than 0.01 and find the fraction of Compton-thick AGN to be 65 per cent. However, they point out that [O III]-based selection results an Eddington bias that would naively lower the observed $L_X/L_{[\text{O III}]}$ ratios and estimate that the true fraction is likely closer to 50% on the basis of the observed L_X/L_{MIR} values for their sample.

The V10 sample is selected from the catalog of 291 type 2 quasars in Z03, with $L_{[\text{O III}]} > 10^{9.28} L_\odot$ (note that the [O III] luminosities used by V10 are from Z03, which are slightly different from the those given by R08 due to a different OIII line fitting procedure). This sample had complete X-ray coverage. However, the R08 catalog is significantly larger, with 887 type 2 quasars selected by applying the same criteria to newer and more extensive SDSS data. This increase in sample size, plus the larger range in $L_{[\text{O III}]}$ that we have probed means that our sample is not complete with respect to the optical selection. Thus, it is necessary to discuss how the completeness may affect our estimation of the fraction of Compton-thick AGNs. In Figure 13, we show the completeness of our sample in the catalog of R08, which is the number of AGNs in our sample above a given [O III] luminosity divided by the number of AGNs in R08 sample above the same [O III] luminosity. Although our sample only covers a small fraction ($\sim 8\%$) of the parent sample in Reyes et al. (2008) over most of the [O III] luminosity range, the completeness rises rapidly at higher luminosities, reaching over $> 20\%$ in the luminosity range studied by V10 ($L_{[\text{O III}]} > 10^{9.10} L_\odot$ according to the new measurement of [O III] luminosity by Reyes et al. 2008).

If we limit the [O III] luminosity range of our sample to that in V10, the Compton-thick fraction becomes 56% (19 out of 34) with $L_{[\text{O III}]} > 10^{9.10} L_\odot$, consistent with the fraction reported in V10. While with [O III] luminosity above $10^{9.50} L_\odot$, the Compton-thick fraction is 53% (8 out of 15).

Only 13 out of the 72 quasars in our sample were initially targeted observations by *Chandra* and *XMM-Newton* and were not obviously selected independently of their X-ray properties. The others are either serendipitous objects in the field of view or were observed in X-rays based on their optical properties (i.e., [O III] luminosity). Thus, the majority of our sample were not observed in X-rays based on their known X-ray properties. From this point of view, we can safely claim that our sample is not X-ray biased.

5. Summary

We have presented the hard (2-10 keV) X-ray spectral properties of 72 type 2 quasars in the redshift range of $z \sim 0.05 - 0.73$ from *Chandra* and *XMM-Newton* archival data, which are selected based on their [O III] λ 5007 emission line luminosity. This is the largest sample of obscured quasars studied in X-rays to date. Their observed [O III] luminosities range from 10^8 - $10^{10.3} L_{\odot}$.

Of these 72 objects, 18 have limited photons detected, and we gave the 3- σ upper limits to their X-ray fluxes. For the remainder, we have fitted their X-ray spectra by assuming a single absorbed power-law to probe their spectral slope and circumnuclear obscuration. Twenty three sources have more than 100 photons collected so that we used a more complicated model (double- absorber power-law) to re-do their spectral fits. We also fit the Fe K α fluorescent emission line in individual sources. For the others, we grouped them in four bins according to their observed $L_X/L_{[\text{O III}]}$ ratios and $L_{[\text{O III}]}$ and jointly fit their spectra to investigate the Fe K α feature. We also used a more physically realistic model to simulate the X-ray spectrum, which included partial covering by the absorber and the effects of Compton scattering. Our main results are summarized as follows:

1. For the 54 sources fitted with absorbed power-law we find the average value for the power-law index is $\langle \Gamma \rangle = 1.87 \pm 0.74$. The average column density of our sample from the direct spectral fit is $\log N_{\text{H}} = 23.0 \pm 0.9 \text{ cm}^{-2}$.
2. The distribution of the $L_X/L_{[\text{O III}]}$ ratio of our type 2 quasar sample agrees with that of local lower luminosity type 2 Seyferts studied previously, indicating that they are experiencing similar amounts of X-ray obscuration. Based on the small ratios of $L_X/L_{[\text{O III}]}$, we found that the single-absorber power-law model underestimates the intrinsic X-ray obscuration. The double-absorber power-law model we applied to the 23 brightest sources also gave a higher column density than the single-absorber model.
3. We constructed a more physically realistic model with partial covering of the central source and Compton scattering to simulate the intrinsic column densities that produced the observed low $L_X/L_{[\text{O III}]}$ ratio. We find that about half of our sample have simulated column densities one order of magnitude higher than from their single power-law spectral fits, but a significantly better agreement with the double power-law model results.
4. We investigated the Fe K α features directly detected in 11 individual sources and the rest in groups by stacking (jointly fitting) their spectra. The anti-correlation between the iron line equivalent width and the $L_X/L_{[\text{O III}]}$ ratio confirms the relationship studied

previously (Krolik & Kallman 1987; Bassani et al. 1999; LaMassa et al. 2009). Also, we find that the iron line luminosity correlates well with the [O III] line luminosity, extending the relation seen in type 2 Seyferts to higher luminosities. These correlations illustrate that the weak observed hard X-ray emission is due to the heavy absorption around the central SMBH, not due to intrinsically weak X-ray emission. The consistency of these correlations with those found in low- luminosity Seyfert galaxies supports the standard model of AGN at the high luminosity end.

5. By combining our analysis with results for type 2 Seyferts from LaMassa et al. (2009, 2011) we found no dependence of the simulated absorbing column densities on AGN luminosity. We also found a nearly linear relationship between the [OIII] and X-ray luminosities. These results show that the amount of X-ray obscuration does not depend significantly on AGN luminosity (over a range in luminosity of over three orders-of-magnitude).
6. Based on the observed $L_X/L_{[\text{O III}]}$ ratio and the simulated column densities, we found that about half of the total 72 quasars would be classified as Compton-thick AGNs. When limiting the $L_{[\text{O III}]}$ range to higher values, the Compton-thick fraction does not change significantly. However, more accurate quantification of the Compton-thick fraction and its dependence on intrinsic luminosity requires a larger sample.

The first focusing high energy X-ray mission, the Nuclear Spectroscopic Telescope Array (*NuSTAR*), will be launched soon. *NuSTAR* will carry out a two-year baseline survey, which will resolve the XRB above 10 keV. This survey will surely improve our estimation of the intrinsic obscuration of obscured AGNs, especially the Compton-thick ones.

Appendix

A. Objects studied in other literature

30 quasars in our sample were also found in papers of X-ray studies of Type 2 AGN (V04; V06; V10; L09 and P06), which are flagged in the last column of Table 1. There are 17 objects studied in V04, but only SDSS J1226+0131 has *XMM* data and others are observed by *ROSAT*. Two objects (SDSS J0115+0015 and SDSS J0243+0006) in P06 were included in Z03, but the [O III] luminosity cut excludes them in R08. Therefore, we remove these two objects in this paper.

Objects with limited photon counts. SDSS J0120–0050, SDSS J0134+0014, SDSS J0319–0058, SDSS J0737+4021, SDSS J1027+0032, SDSS J1446+0113, SDSS J1517+0331 and SDSS J2358–0022 have their X-ray luminosity given as a $3\text{-}\sigma$ upper limit in our work (see Table 3). However, the de-absorbed X-ray luminosity of these sources in V06 and V10 are not listed as upper limits. The luminosities are based on directly converting from their observed 2-8 keV count rates.

SDSS J0149–0048, SDSS J0815+4304, SDSS J0842+3625, SDSS J0921+4531 and SDSS J1157+6003 have upper limits on the observed flux and derived X-ray luminosity given in our work, V06 and V10. However, we find that our values are systematically one order of magnitude larger than those in V04, V06, V10. This difference is due to our assumption of an intrinsic column density of 10^{23} cm^{-2} in converting the source count rates to flux, while only Galactic absorption was assumed by them.

SDSS J0050-0039. The spectral parameters given by V06 are $N_{\text{H}} = 3.75 \times 10^{23} \text{ cm}^{-2}$ and $\Gamma = 1.78$, and the derived de-absorbed 2-10 keV luminosity is $7.2 \times 10^{44} \text{ erg s}^{-1}$. These values are consistent with our analysis of the same *Chandra* observation (Obs ID: 5694), and we also derive the observed 2-10 keV luminosity of $1.8 \times 10^{44} \text{ erg s}^{-1}$.

SDSS J0123+0044. This object has enough photons to constrain the spectral parameters. V10 fixed the photon index at $\Gamma = 2$ and derived the column density of $N_{\text{H}} = 1.44 \times 10^{23} \text{ cm}^{-2}$, which is 1.5 times of our value. The photon index in our double-absorber power-law fitting is $\Gamma = 1.06$.

SDSS J0157+0053. The *Chandra* observation (Obs ID:7750) is studied by both V10 and us. The de-absorbed X-ray luminosity of this *Chandra* observation from our work is one order of magnitude larger than that given by them. However, we also found an *XMM* observation available, which has many more photon counts than the *Chandra* data to constrain the spectral parameters. The result of multiple observations is shown in Appendix B.

SDSS J0210-1001. P06 presented the spectral properties of the object by analyzing the *XMM* observation (Obs ID: 0204340201), which gives a column density of $N_{\text{H}} = 2.3 \times 10^{22} \text{ cm}^{-2}$ and a flat photon index of $\Gamma = 0.46$. V06 re-analyzed the data but only gave the de-absorbed 2-10 keV luminosity, which is close to the value from P06. We have similar results in this paper.

SDSS J0801+4412. We obtain similar spectral parameters and flux for this object as P06 did. The column density given by V06 is $N_{\text{H}} = 4.3 \times 10^{23} \text{ cm}^{-2}$, while it is $1.7 \times 10^{23} \text{ cm}^{-2}$ in our work. Thus, the de-absorbed X-ray luminosity is about 5 times higher than the values in P06 and this paper.

SDSS J0812+4018. The best-fit photon index and absorption of SDSS J0812+4018 in V10 are $\Gamma = 2.6$ and $N_{\text{H}} = 2.14 \times 10^{22} \text{ cm}^{-2}$. Our results are $\Gamma = 1.91$ and $N_{\text{H}} = 9.3 \times 10^{21} \text{ cm}^{-2}$, which has a flatter spectral slope and slightly smaller obscuration.

SDSS J0920+4531. Neither V10 nor our work is able to constrain the column density from the spectral fit. They fixed the photon index at $\Gamma = 2$ and our value is $\Gamma = 1.38$, and our value of the derived X-ray luminosity is twice as large as theirs.

SDSS J1039+6430. Very limited photons are detected, and the spectral fit by both V10 and us fixed the photon index and left the column density as the Galactic value. Our results are similar to the values in V10.

SDSS J1153+0326. V06 fitted the spectrum firstly by a power-law and Galactic absorption only, and they got a flat photon index of $\Gamma = 0.56$. This is consistent with our result in Table 2. They then fixed the index at $\Gamma = 2$ and got an absorption of $N_{\text{H}} = 1.54 \times 10^{22} \text{ cm}^{-2}$. In our double power-law model fitting, the photon index is $\Gamma = 1.54$ and the column density at the redshift of this source is $N_{\text{H}} = 8.9 \times 10^{22} \text{ cm}^{-2}$.

SDSS J1218+4706. Our spectral fit results are very similar to those from L09. Both works performed the double-absorber power-law model in the spectral fitting.

SDSS J1226+0131. The *XMM* observation (Obs ID: 0110990201) is studied by both V04 and P06. The best-fitting spectrum of SDSS J1226+0131 in V04 gives a flat photon index of $\Gamma = 1.3$ and column density $N_{\text{H}} = 1.26 \times 10^{22} \text{ cm}^{-2}$. In P06, the simple power-law model fitting gives $\Gamma = 1.41$ and $N_{\text{H}} = 2.0 \times 10^{22} \text{ cm}^{-2}$. P06 also used a two-absorber model by assuming partial covering, and the other absorber has a column density of $N_{\text{H}} = 8.7 \times 10^{23} \text{ cm}^{-2}$, while we get a similar value in our double power-law model fitting ($N_{\text{H}} = 1.2 \times 10^{24} \text{ cm}^{-2}$). The observed hard X-ray luminosity is consistent with the two papers.

SDSS J1228+0050. The column density from the spectral fit by V10 is $N_{\text{H}} = 1.52 \times 10^{23} \text{ cm}^{-2}$, which is very close to our value of $N_{\text{H}} = 1.32 \times 10^{23} \text{ cm}^{-2}$. The photon index given

by both works is slightly different: $\Gamma = 1.9$ in their paper and 1.55 in ours.

SDSS J1232+0206. This object has fewer than 10 source counts detected. P06 fixed both photon index and column density ($\Gamma = 1.7$ and $N_{\text{H}} = 1.0 \times 10^{23} \text{ cm}^{-2}$) in the spectral fitting. We only fixed the index at 1.7 and N_{H} was constrained to be $7.45 \times 10^{22} \text{ cm}^{-2}$. Our derived flux value is consistent with P06 within a factor of two.

SDSS J1238+0927. Our spectral fit results are very similar to those from L09. Both works performed the double-absorber power-law model in the spectral fitting.

SDSS J1641+3858. The spectral properties obtained by P06 are very close to the values in our paper. V06 got a column density slightly higher but still consistent with our value.

SDSS J2358-0009. This object was considered to be a serendipitous source with a large off-axis angle in the *Chandra* observation (Obs ID: 5699). Only upper limits of flux and luminosity were given in V06 due to the very limited photon counts. This data set is ruled out for this object by the search radius described in Section 2. Instead, we found that it is covered by two *XMM* observation (see Table 1). We performed a moderate-quality spectral fit by using the *XMM* data.

B. Objects with multiple observations

SDSS J0056+0032. It was observed by *XMM* (Obs ID: 0303110401) and *Chandra* (Obs ID: 7746) in 2005 and 2008, respectively. We used a simple power-law to fit the spectra, and the spectral parameters for each observation are given in Table 2. The *XMM* observation had 59 total photons detected, which allows us to perform a moderate quality spectral fit. The *Chandra* observation detected only 6 photons, and we fixed the photon index as 1.7 and derived the hard X-ray luminosity (not the $3\text{-}\sigma$ upper limit), which is consistent with the results from the *XMM* data. The simultaneous fit of both observations gives a photon index of 1.64, which is slightly flatter than 1.84 from *XMM*.

SDSS J0157-0053. The *Chandra* observation (Obs ID: 7750) has 23 photons detected, which allows a moderate quality spectral fit. The photon index is $\Gamma = -0.47$ for this *Chandra* observation. *XMM* observation (Obs ID: 0303110101) detected ~ 500 photons and the spectral fit gives $\Gamma = 1.64$. Due to the insufficient photon counts in *Chandra* observation, we use the spectral properties and derived flux from the *XMM* observation in the sample statistics.

SDSS J0758+3923. There are two *XMM* observations available for this object with Obs ID: 0406740101 and 0305990101. No significant flux variability is observed. The spectral fit

parameters for both individual and combined observations are listed in Table 2. The spectral plot of *XMM*- 0406740101 is shown in Figure 1, and Figure 14 shows the simultaneous spectral fit for multi-observations.

SDSS J0834+5534. Also known as 4C 55.16. Two *Chandra* observations (Obs ID: 1645 and 4940) and one *XMM* observation (Obs ID: 0143653901) are found to cover 0834+5534. The *XMM* imaging shows a point-like morphology of this object, but it is extended in the *Chandra* observation. The radii of extraction circles on *Chandra* and *XMM* images are 2.5'' and 38'', respectively. The 2-10 keV flux measured from *XMM* data is one order of magnitude higher than that from *Chandra* observations (see Table 2). Since it is radio-loud, the extended emission is probably due to the jets. Therefore, we use the results of the 2.5'' extraction region in *Chandra* data. A simultaneous spectral fit of both *Chandra* observations is shown in Figure 14.

SDSS J0900+2053. Two *Chandra* observations (Obs ID: 10463 and 7897) and one *XMM* observation (Obs ID: 0402250701) are found to cover 0900+2053. The *Chandra* observations show an extended morphology in X-ray emission. The star formation rate of the galaxy is $12.5 M_{\odot} \text{ yr}^{-1}$ given by the MPA/JHU DR7 of SDSS. We extracted the spectra from concentric regions with radii of 2.5'', 10'' and 20''. The soft X-ray fluxes of the two larger regions are 7 and 10 times of that in the 2.5'' region, while the hard X-ray fluxes of the two larger regions are only 2 and 3 times of that in the smallest region. Thus, the extended emission is dominated by soft X-ray photons from star formation. We use the 2.5'' region to estimate the quasar emission in this paper. Simultaneous spectral fit of both *Chandra* observations is shown in Figure 14.

SDSS J0913+4056. This is a hyperluminous infrared galaxy. Two *Chandra* observations (Obs ID: 10445 and 509) and one *XMM* observation (Obs ID: 0147671001) are found to cover SDSS J0913+4056. Like SDSS J0900+2053, soft X-ray photons dominate the extended emission, and we use the 2.5'' region for the spectral analysis of quasar emission. A simultaneous spectral fit of both *Chandra* observations is shown in Figure 14. Our spectral analysis results are consistent with the original papers which studied these three observations (Iwasawa et al. 2001; Piconcelli et al. 2007; Vignali et al. 2011).

SDSS J1227+1248. Three *Chandra* observations (Obs ID: 5912, 9509 and 9510) and one *XMM* observation (Obs ID: 0210270101) have SDSS J1227+1248 covered in the field of view. The simultaneous fit of three *Chandra* data sets is shown in Figure 14. However, we only use the *XMM* observation in the double power-law spectral fit to derive the spectral properties.

SDSS J1311+2728. This object is observed by *XMM* (Obs ID: 0021740201) and *Chan-*

dra (Obs ID: 12735) with exposure times of 44 ks and 8 ks, respectively. The *XMM* observation has 588 total X-ray photons detected, while only 19 photons are captured by *Chandra*. Therefore, the spectral properties of SDSS J1311+2728 presented in this paper are from the *XMM* observation.

SDSS J2358-0009. This object is observed by two *XMM* observations (Obs ID: 0303110301 and 0303110801). The simultaneous fit of both observations is shown in Figure 14.

REFERENCES

- Akylas, A., Georgantopoulos, I., Georgakakis, A., Kitsionas, S., & Hatziminaoglou, E. 2006, *A&A*, 459, 693
- Antonucci, R. 1993, *ARA&A*, 31, 473
- Balucinska-Church, M., & McCammon, D. 1992, *ApJ*, 400, 699
- Barger, A. J., Cowie, L. L., Mushotzky, R. F., et al. 2005, *AJ*, 129, 578
- Bassani, L., Dadina, M., Maiolino, R., et al. 1999, *ApJS*, 121, 473
- Cash, W. 1979, *ApJ*, 228, 939
- de Rosa, A., Panessa, F., Bassani, L., et al. 2012, *MNRAS*, 2261
- Dickey, J. M., & Lockman, F. J. 1990, *ARA&A*, 28, 215
- Fiore, F., Grazian, A., Santini, P., et al. 2008, *ApJ*, 672, 94
- Gilli, R., Comastri, A., & Hasinger, G. 2007, *A&A*, 463, 79
- Hao, L., Strauss, M. A., Fan, X., et al. 2005, *AJ*, 129, 1795
- Heckman, T. M., Ptak, A., Hornschemeier, A., & Kauffmann, G. 2005, *ApJ*, 634, 161
- Isobe, T., & Feigelson, E. D. 1990, *BAAS*, 22, 917
- Isobe, T., Feigelson, E. D., & Nelson, P. I. 1986, *ApJ*, 306, 490
- Iwasawa, K., Fabian, A. C., & Ettori, S. 2001, *MNRAS*, 321, L15
- Jin, C., Ward, M., & Done, C. 2012, *arXiv:1203.0239*
- Kraft, R. P., Burrows, D. N., & Nousek, J. A. 1991, *ApJ*, 374, 344
- Krolik, J. H., & Kallman, T. R. 1987, *ApJ*, 320, L5
- LaMassa, S. M., Heckman, T. M., Ptak, A., et al. 2011, *ApJ*, 729, 52
- LaMassa, S. M., Heckman, T. M., Ptak, A., et al. 2010, *ApJ*, 720, 786
- LaMassa, S. M., Heckman, T. M., Ptak, A., et al. 2009, *ApJ*, 705, 568 (L09)
- Lavalley, M., Isobe, T., & Feigelson, E. 1992, *Astronomical Data Analysis Software and Systems I*, 25, 245

- Lawrence, A., & Elvis, M. 2010, *ApJ*, 714, 561
- Marconi, A., Risaliti, G., Gilli, R., et al. 2004, *MNRAS*, 351, 169
- Markwardt, C. B., Tueller, J., Skinner, G. K., et al. 2005, *ApJ*, 633, L77
- Melendez, M., Weaver, K. A., Mushotzky, R. F., et al. 2009, *Bulletin of the American Astronomical Society*, 41, #421.10
- Mulchaey, J. S., Koratkar, A., Ward, M. J., et al. 1994, *ApJ*, 436, 586
- Nandra, K., Laird, E. S., Adelberger, K., et al. 2005, *MNRAS*, 356, 568
- Piconcelli, E., Fiore, F., Nicastro, F., et al. 2007, *A&A*, 473, 85
- Ptak, A., Heckman, T., Levenson, N. A., Weaver, K., & Strickland, D. 2003, *ApJ*, 592, 782
- Ptak, A., Zakamska, N. L., Strauss, M. A., et al. 2006, *ApJ*, 637, 147 (P06)
- Reyes, R., Zakamska, N. L., Strauss, M. A., et al. 2008, *AJ*, 136, 2373 (R08)
- Rigby, J. R., Diamond-Stanic, A. M., & Aniano, G. 2009, *ApJ*, 700, 1878
- Risaliti, G. 2002, *A&A*, 386, 379
- Sazonov, S., Revnivtsev, M., Krivonos, R., Churazov, E., & Sunyaev, R. 2007, *A&A*, 462, 57
- Sazonov, S. Y., & Revnivtsev, M. G. 2004, *A&A*, 423, 469
- Spergel, D. N., Verde, L., Peiris, H. V., et al. 2003, *ApJS*, 148, 175
- Teng, S. H., Wilson, A. S., Veilleux, S., et al. 2005, *ApJ*, 633, 664
- Tozzi, P., et al. 2006, *A&A*, 451, 457
- Treister, E., Krolik, J. H., & Dullemond, C. 2008, *ApJ*, 679, 140
- Treister, E., & Urry, C. 2005, *ApJ*, 630, 115
- Treister, E., & Urry, C. M. 2011, *arXiv:1112.0320*
- Tueller, J., Mushotzky, R. F., Barthelmy, S., et al. 2008, *ApJ*, 681, 113
- Turner, T. J., George, I. M., Nandra, K., & Mushotzky, R. F. 1997, *ApJS*, 113, 23
- Ueda, Y., Akiyama, M., Ohta, K., & Miyaji, T. 2003, *ApJ*, 598, 886

- Vignali, C., Piconcelli, E., Lanzuisi, G., et al. 2011, MNRAS, 416, 2068
- Vignali, C., Alexander, D. M., Gilli, R., & Pozzi, F. 2010, MNRAS, 404, 48 (V10)
- Vignali, C., Alexander, D. M., & Comastri, A. 2006, MNRAS, 373, 321 (V06)
- Vignali, C., Alexander, D. M., & Comastri, A. 2004, MNRAS, 354, 720 (V04)
- Winter, L. M., Mushotzky, R. F., Reynolds, C. S., & Tueller, J. 2009, ApJ, 690, 1322
- Worsley, M. A., Fabian, A. C., Bauer, F. E., et al. 2006, MNRAS, 368, 1735
- Yaqoob, T. 1997, ApJ, 479, 184
- York, D. G., Adelman, J., Anderson, J. E., Jr., et al. 2000, AJ, 120, 1579
- Zakamska, N. L., Schmidt, G. D., Smith, P. S., et al. 2005, AJ, 129, 1212
- Zakamska, N. L., Strauss, M. A., Heckman, T. M., Ivezić, Ž., & Krolik, J. H. 2004, AJ, 128, 1002
- Zakamska, N. L., Strauss, M. A., Krolik, J. H., et al. 2003, AJ, 126, 2125 (Z03)
- Zakamska, N. L., Strauss, M. A., Krolik, J. H., et al. 2006, AJ, 132, 1496

Table 1. SDSS type 2 AGN observed with *Chandra* or *XMM-Newton*

ID J2000 coordinates (1)	Galactic $N_{\text{H,G}}$ ($\times 10^{20} \text{ cm}^{-2}$) (2)	z (3)	$\log(L_{[\text{O III}]} / L_{\odot})$ (4)	Observation ID (5)	Exposure (ks) (6)	Date mm/dd/yy (7)	off-axis angle (') (8)	ref. (9)
SDSS J001111.97+005626.3	2.89	0.4094	8.67	<i>XMM</i> -0403760301	19.9 (P) 25.1 (M1) 25.1 (M2)	08/07/07	4.8	
SDSS J002852.86+001433.5	2.66	0.3103	8.08	<i>XMM</i> -0403160101	0.84 (P) 1.4 (M1) 1.5 (M2)	06/29/07	7.9	
SDSS J005009.81+003900.6	2.57	0.7276	10.06	<i>Chandra</i> -5694	7.96	08/28/05		<i>b</i>
SDSS J005621.72+003235.8	2.86	0.4840	9.25	<i>XMM</i> -0303110401	8.7 (P) 11.4 (M1) 11.4 (M2)	07/16/05		
				<i>Chandra</i> -7746	9.91	02/08/08		<i>c</i>
SDSS J012032.21+005502.0	3.69	0.6010	8.85	<i>Chandra</i> -7747	10.19	02/18/07		<i>c</i>
SDSS J012341.47+004435.9	3.24	0.3990	9.14	<i>Chandra</i> -6802	9.96	02/07/06		<i>c</i>
SDSS J013416.34+001413.6	2.91	0.5559	9.53	<i>Chandra</i> -7748	10.0	09/10/07		<i>c</i>
SDSS J014932.53+004803.7	2.85	0.5669	9.29	<i>Chandra</i> -7749	10.1	08/30/07		<i>c</i>
SDSS J015716.92+005304.8	2.58	0.4223	9.19	<i>Chandra</i> -7750	9.7	06/18/07		<i>c</i>
				<i>XMM</i> -0303110101	9.9 (P) 12.7 (M1) 12.7 (M2)	07/14/05		
SDSS J021047.01+100152.9	2.17	0.5401	9.87	<i>XMM</i> -0204340201	9.1 (P) 11.6 (M1) 11.6 (M2)	01/12/04		<i>b, e</i>
SDSS J030425.69+000740.9	7.05	0.5557	9.26	<i>XMM</i> -0203160201	15.4 (P) 14.9 (M1) 14.9 (M2)	07/19/04	8.1	
SDSS J031950.54+005850.6	6.05	0.6261	9.59	<i>Chandra</i> -5695	11.64	03/10/05		<i>b</i>
SDSS J033746.73+003509.7	8.31	0.4096	8.6	<i>XMM</i> -0117890901	48.6 (P) 1.8 (M1) 54.0 (M2)	02/18/00	8.1	
SDSS J073745.88+402146.5	6.18	0.6142	9.31	<i>Chandra</i> -7751	9.45	02/03/07		<i>c</i>
SDSS J075820.98+392336.0	5.22	0.2160	9.02	<i>XMM</i> -0406740101	10.89 (P) 14.22 (M1) 14.24 (M2)	10/22/06	4.1	
				<i>XMM</i> -0305990101	2.0 (P) 7.9 (M1) 7.9 (M2)	04/18/06	6.1	
SDSS J080154.24+441233.9	4.79	0.5561	9.64	<i>Chandra</i> -5248	9.94	11/27/03		<i>b, e</i>
SDSS J081253.10+401859.9	5.16	0.5512	9.39	<i>Chandra</i> -6801	10.02	12/11/05		<i>c</i>
SDSS J081507.42+430427.2	5.02	0.5099	9.44	<i>Chandra</i> -5696	8.28	12/27/05		<i>b</i>
SDSS J083454.89+553421.1	4.14	0.2414	8.69	<i>Chandra</i> -1645	9.01	10/17/01		
				<i>Chandra</i> -4940	95.96	01/03/04		
				<i>XMM</i> -0143653901	6.3 (P) 9.6 (M1) 9.6 (M2)	10/09/03	13.1	
SDSS J083945.98+384319.0	3.55	0.4246	8.60	<i>XMM</i> -0502060201	15.35 (P) 18.65 (M1) 18.68 (M2)	10/16/07	10.8	
SDSS J084041.08+383819.8	3.45	0.3132	8.45	<i>XMM</i> -0502060201	15.36 (P) 18.8 (M1) 18.75 (M2)	10/16/07		
SDSS J084234.94+362503.1	3.41	0.5615	10.02	<i>Chandra</i> -532	19.68	10/21/99	5.4	<i>b, e</i>
SDSS J085331.39+175347.3	2.94	0.1865	8.92	<i>XMM</i> -0305480301	23.28 (P) 68.58 (M1) 68.39 (M2)	10/28/05	11.4	
SDSS J085554.47+370900.4	2.93	0.3567	8.84	<i>Chandra</i> -6807	10.46	02/17/06	4.93	
SDSS J090037.09+205340.2	3.39	0.2357	8.98	<i>Chandra</i> -10463	41.18	02/24/09		
				<i>Chandra</i> -7897	9.05	12/23/06	1.3	
				<i>XMM</i> -0402250701	9.9 (P) 15.7 (M1) 15.7 (M2)	04/13/07		
SDSS J091345.48+405628.2	1.82	0.4409	10.33	<i>Chandra</i> -509	9.17	11/03/99		

Table 1—Continued

ID J2000 coordinates (1)	Galactic $N_{\text{H,G}}$ ($\times 10^{20} \text{ cm}^{-2}$) (2)	z (3)	$\log(L_{[\text{O III}]} / L_{\odot})$ (4)	Observation ID (5)	Exposure (ks) (6)	Date mm/dd/yy (7)	off-axis angle (') (8)	ref. (9)
				<i>Chandra</i> -10445	76.16	01/06/09		
				<i>XMM</i> -0147671001	10.2 (P) 13.52 (M1) 13.55 (M2)	04/24/03	1.1	
SDSS J092014.10+453157.3	1.51	0.4025	9.15	<i>Chandra</i> -6803	10.18	03/05/06		<i>c</i>
SDSS J092152.45+515348.1	1.42	0.5877	9.41	<i>Chandra</i> -7752	10.18	09/27/07		<i>c</i>
SDSS J092318.06+010144.8	3.32	0.3873	8.77	<i>XMM</i> -0551201001	23.1 (P) 26.7 (M1)	11/06/08		
SDSS J092438.24+302837.1	1.94	0.2727	8.80	<i>XMM</i> -0553440601	4.37 (P) 6.51 (M1)	11/22/08	10.3	
SDSS J093952.74+355358.0	1.43	0.1366	8.75	<i>XMM</i> -0021740101	26.6 (P) 33.9 (M1) 33.9 (M2)	10/27/01		
SDSS J094506.39+035551.1	3.71	0.1559	8.60	<i>XMM</i> -0201290301	24.9 (P) 37.0 (M1) 37.0 (M2)	05/19/04	10.0	
SDSS J100327.93+554153.9	0.775	0.1460	8.24	<i>XMM</i> -0110930201	17.1 (P) 24.5 (M1) 24.5 (M2)	04/13/01	13.2	
SDSS J102229.00+192939.0	2.36	0.4063	9.13	<i>Chandra</i> -4907	7.28	03/31/05		
SDSS J102746.03+003205.0	4.47	0.6137	9.46	<i>Chandra</i> -7883	10.04	01/13/07		<i>c</i>
SDSS J103408.59+600152.2	0.69	0.0511	8.81	<i>XMM</i> -0306050701	8.8 (P) 11.4 (M1) 11.4 (M2)	04/04/05	1.2	
SDSS J103456.40+393940.0	1.47	0.1507	8.91	<i>XMM</i> -0506440101	11.9 (P) 15.0 (M1) 15.0 (M2)	05/01/02	4.6	
SDSS J103951.49+643004.2	1.18	0.4018	9.43	<i>Chandra</i> -7753	10.04	02/04/07		<i>c</i>
SDSS J104426.70+063753.8	2.82	0.2104	8.16	<i>XMM</i> -0405240901	23.98 (P) 30.96 (M1) 30.95 (M2)	06/05/07	5.5	
SDSS J110621.96+035747.1	4.58	0.2424	9.01	<i>Chandra</i> -6806	10.16	02/02/06		
SDSS J111907.01+600430.8	0.71	0.2642	8.28	<i>XMM</i> -0502780201	9.6 (P) 13.5 (M1) 13.5 (M2)	05/20/07		
SDSS J113153.75+310639.7	1.96	0.3727	8.52	<i>XMM</i> -0102040201	17.16 (M1) 23.34 (M2)	11/22/00	12.1	
SDSS J114544.99+024126.9	2.21	0.1283	8.19	<i>XMM</i> -0551022701	13.8 (P)	06/15/08	8.0	
SDSS J115138.24+004946.4	2.26	0.1951	8.40	<i>Chandra</i> -7735	4.70	07/09/07		
SDSS J115314.36+032658.6	1.89	0.5748	9.64	<i>Chandra</i> -5697	8.28	04/10/05		<i>b</i>
SDSS J115718.35+600345.6	1.65	0.4903	9.61	<i>Chandra</i> -5698	7.06	06/06/06		<i>b</i>
SDSS J121839.40+470627.7	1.17	0.0939	8.56	<i>XMM</i> -0203270201	14.2 (P) 33.3 (M1) 35.0 (M2)	06/01/04	6.0	<i>d</i>
SDSS J122656.40+013124.3	1.84	0.7321	9.8	<i>XMM</i> -0110990201	21.3 (P) 28.6 (M1) 28.6 (M2)	06/23/01	5.0	<i>a, e</i>
SDSS J122709.84+124854.5	2.64	0.1945	8.5	<i>XMM</i> -0210270101	21.95 (P) 26.16 (M1) 26.16 (M2)	12/19/04	3.8	
				<i>Chandra</i> -5912	32.64	03/09/05	4.2	
				<i>Chandra</i> -9509	25.81	04/14/08	6.7	
				<i>Chandra</i> -9510	25.22	04/14/08	7.5	
SDSS J122845.74+005018.7	1.88	0.5750	9.28	<i>Chandra</i> -7754	9.54	03/12/07		<i>c</i>
SDSS J123215.81+020610.0	1.80	0.4800	9.62	<i>Chandra</i> -4911	9.73	04/21/05		<i>b, e</i>
SDSS J123843.02+092744.0	1.87	0.0892	8.51	<i>XMM</i> -0504100601	17.4 (P) 21.3 (M1) 21.3 (M2)	12/09/07	1.7	<i>d</i>
SDSS J124302.48+122022.8	2.34	0.4852	9.09	<i>Chandra</i> -11322	10.62	02/28/10	3.4	
SDSS J124337.34-023200.2	2.03	0.2814	8.88	<i>Chandra</i> -6805	10.16	04/25/06		

Table 1—Continued

ID	Galactic $N_{\mathrm{H,G}}$	z	$\log(L_{[\mathrm{O\ III}]}/L_{\odot})$	Observation	Exposure	Date	off-axis	ref.
J2000 coordinates	($\times 10^{20} \mathrm{cm}^{-2}$)			ID	(ks)	mm/dd/yy	angle (')	
(1)	(2)	(3)	(4)	(5)	(6)	(7)	(8)	(9)
SDSS J130128.76−005804.3	1.59	0.2455	9.12	<i>Chandra</i> -6804	10.18	05/30/06		
SDSS J131104.36+272813.4	0.98	0.2398	8.46	<i>XMM</i> -0021740201	40.3 (P) 43.7 (M1) 43.7 (M2)	12/12/02		
				<i>Chandra</i> -12735	7.95	11/17/10		
SDSS J132419.88+053704.6	2.26	0.2027	8.49	<i>XMM</i> -0200660301	10.7 (P) 10.0 (M1) 10.2 (M2)	07/11/04	1.7	
SDSS J132946.20+114009.3	1.93	0.5596	9.36	<i>XMM</i> -0041180801	15.6 (P) 22.3 (M1) 22.3 (M2)	12/30/01	7.8	
SDSS J133735.02−012815.7	2.41	0.3292	8.71	<i>XMM</i> -0502060101	2.4 (M2)	07/11/07		
SDSS J134733.36+121724.3	1.90	0.1204	8.65	<i>Chandra</i> -836	27.95	02/24/00		
SDSS J141120.52+521210.0	1.33	0.4617	8.41	<i>Chandra</i> -2254	92.1	05/18/01		
SDSS J143027.66−005614.9	3.35	0.3177	8.42	<i>XMM</i> -0502060301	1.36 (P) 4.96 (M1) 4.91 (M2)	08/03/07		
SDSS J143156.38+325137.7	1.07	0.4198	9.52	<i>Chandra</i> -4264	5.02	04/01/03	2.6	
				<i>Chandra</i> -10457	34.58	10/30/08	6.0	
SDSS J144642.29+011303.0	3.55	0.7259	9.54	<i>Chandra</i> -7755	10.18	03/22/07		<i>c</i>
SDSS J144920.72+422101.3	1.53	0.1784	8.85	<i>Chandra</i> -5717	4.36	10/04/05		
SDSS J150719.93+002905.1	4.48	0.1819	8.98	<i>XMM</i> -0305750801	10.5 (P) 13.4 (M1) 13.4 (M2)	07/20/05	1.1	
SDSS J151711.47+033100.2	3.78	0.6128	9.10	<i>Chandra</i> -7756	10.04	03/28/07		<i>c</i>
SDSS J160641.42+272556.9	3.89	0.5411	9.44	<i>XMM</i> -0304070701	2.24 (M1) 1.86 (M2)	07/29/05	9.2	
SDSS J164131.73+385840.9	1.16	0.5957	10.04	<i>XMM</i> -0204340101	12.2 (P) 16.8 (M1) 17.1 (M2)	08/20/04		<i>b, e</i>
SDSS J171350.32+572954.9	2.48	0.1128	8.95	<i>XMM</i> -0305750401	6.2 (P) 8.7 (M1) 8.7 (M2)	06/23/05		
SDSS J235818.86−000919.4	3.25	0.4025	9.27	<i>XMM</i> -0303110301	1.87 (P) 5.76 (M1) 5.73 (M2)	12/04/05		
				<i>XMM</i> -0303110801	6.9 (P) 9.5 (M1) 9.5 (M2)	06/20/06		<i>b</i>
SDSS J235831.16−002226.5	3.29	0.6277	9.68	<i>Chandra</i> -5699	6.25	08/08/05		<i>b</i>

Note. — Column 1: J2000 coordinate; Column 2: Galactic column density calculated by HEAsoft N_{H} tool; Column 3: redshift; Column 4: $[\mathrm{O\ III}]\lambda 5007\text{\AA}$ line luminosity in units of solar (from Reyes et al. (2008)); Column 5: *Chandra* and *XMM-Newton* observation ID; Column 6: exposure times after filtering in units of ks (for *XMM-Newton* observations, the exposure times are listed separately for PN (P) and MOS1,2 (M1,2) instruments); Column 7: date of observation; Column 8: separation from the center of field of view in units of arcminute; Column 9: references that have the source included: *a*-Vignali et al. (2004) (V04); *b*-Vignali et al. (2006) (V06); *c*-Vignali et al. (2010) (V10); *d*-LaMassa et al. (2009) (L09); *e*-Ptak et al. (2006) (P06).

Table 2. X-ray spectral properties of SDSS type 2 AGN

ID	Total counts and estimated background counts	N_{H} (10^{22} cm^{-2})	Γ	χ^2/dof or c-stat/dof	L_{X} ($10^{44} \text{ erg s}^{-1}$)	$L_{\text{X,in}}$ ($10^{44} \text{ erg s}^{-1}$)	$L_{\text{X}}/L_{[\text{O III}]}$	$L_{\text{X,in}}/L_{[\text{O III}]}$	Compton- thick
(1)	(2)	(3)	(4)	(5)	(6)	(7)	(8)	(9)	(10)
0011+0056	77(62.6)/.../57(31.3)	< 2.70	$0.60^{+1.17}_{-1.15}$	123.3/122	0.031	0.031	1.72	1.72	✓
0050-0039	45(0.4)	$35.5^{+34.7}_{-26.0}$	$1.73^{+1.86}_{-1.66}$	51.0/39	1.83	7.21	4.20	16.37	✓
0056+0032	25(18.4)/16(8.8)/18(10.5)	< 0.96	$1.84^{+2.46}_{-1.41}$	69.3/54	0.04	0.04	0.59	0.59	✓
	6(0.5)	< 0.64	1.7	4.5/4	0.03	0.03	0.44	0.44	
0123+0044	161(0.3)	$6.92^{+3.28}_{-2.80}$	$0.69^{+0.63}_{-0.61}$	115.1/128	1.81	2.44	34.2	46.0	
0157-0053	23(0.2)	< 0.37	$-0.47^{+0.70}_{-0.87}$	17.5/21	0.33	0.33	5.5	5.5	
	351(322.2)/72(47.6)/83(46.3)	< 0.11	$1.64^{+0.81}_{-0.63}$	443.8/439	0.13	0.13	2.2	2.2	
		< 0.08	$0.73^{+0.37}_{-0.41}$	476.4/461					
0210-1001	189(31.2)/78(8.1)/77(8.5)	$3.03^{+2.06}_{-1.42}$	$0.89^{+0.38}_{-0.35}$	325.9/312	1.81	2.0	6.34	7.03	
0304+0007	.../29(18.2)/28(20.3)	$43.4^{+244.6}_{-3.39}$	$2.10^{+2.07}_{-0.39}$	58.1/51	0.31	1.63	4.4	23.0	
0337+0035	.../.../115(36.6)	$1.00^{+1.96}_{-0.07}$	$1.54^{+1.10}_{-0.75}$	4.0/8	0.46	0.50	30.0	32.7	
0758+3923	90(43.7)/20(8.9)/20(9.3)	< 0.24	$1.38^{+0.96}_{-0.70}$	8.6/8	0.02	0.02	0.44	0.44	✓
	85(69.4)/45(38.3)/46(38.3)	$0.26^{+1.11}_{-0.26}$	$2.04^{+2.82}_{-1.15}$	142.1/164	0.07	0.07	1.5	1.5	
		< 0.25	$1.68^{+0.94}_{-0.71}$	21.3/29					
0801+4412	47(2.4)	$17.1^{+13.8}_{-6.6}$	$0.82^{+0.81}_{-0.84}$	70.8/42	0.92	2.10	5.5	12.5	
0812+4018	201(0.8)	$0.93^{+0.45}_{-0.42}$	$1.91^{+0.37}_{-0.36}$	104.9/125	1.56	1.70	16.4	18.0	
0834+5534	174(57.9)	$0.054^{+0.108}_{-0.054}$	$1.64^{+0.36}_{-0.32}$	101.9/113	0.17	0.17	9.0	9.0	
	2967 (3.0)	$0.11^{+0.03}_{-0.03}$	$2.09^{+0.10}_{-0.10}$	126.2/103	0.21	0.22	11.1	11.2	
	2514(238.8)/1079(74.5)/1110(69.9)	$0.12^{+0.02}_{-0.02}$	$2.24^{+0.10}_{-0.09}$	236.2/200	2.67	2.71	142	144	
		$0.12^{+0.02}_{-0.03}$	$2.12^{+0.11}_{-0.10}$	128.6/122					
0839+3843	363(137.6)/133(37.9)/111(41.5)	$2.01^{+1.57}_{-1.05}$	$1.21^{+0.45}_{-0.39}$	54.6/55	1.36	1.56	89	102	
0840+3838	91(64.7)/30(21.9)/29(20.9)	< 0.38	$2.08^{+1.68}_{-1.17}$	130.4/137	0.008	0.008	0.71	0.71	✓
0853+1753	134(28.3)/169(52.9)/124(15.7)	< 0.07	$-0.02^{+1.33}_{-1.25}$	380.8/367	0.081	0.081	2.53	2.53	✓
0855+3709	26(1.6)	$3.27^{+4.66}_{-3.05}$	$1.14^{+1.47}_{-1.29}$	26.6/23	0.23	0.28	8.6	11.3	
0900+2053	2017(2.0)	...	1.11	289.8/78					
	336(0.3)	...	0.53	32.59/13					
	7871(23.6)/3705(7.4)/3098(9.3)	$0.08^{+0.01}_{-0.01}$	$2.07^{+0.05}_{-0.04}$	658.0/537	2.37	2.39	64.7	65.3	
0913+4056	250(50.0)	< 0.02	$1.41^{+0.16}_{-0.15}$	156.9/141	1.50	1.50	1.8	1.8	
	2298 (2.3)	...	$1.37^{+0.11}_{-0.11}$	200.2/88					
	6259(275.4)/2470(86.5)/2574(75.6)	$0.07^{+0.02}_{-0.02}$	$1.88^{+0.06}_{-0.05}$	466.8/425	9.67	9.73	11.8	11.9	
0920+4531	17(2.6)	< 0.31	$1.38^{+1.32}_{-0.93}$	17.1/15	0.04	0.04	0.72	0.72	✓
0923+0101	171(120.2)/38(31.5)/24(25.4)	< 0.08	1.7	188.1/205	0.026	0.026	1.14	1.14	✓
0924+3028	53(38.2)/24(6.2)/...	$23.4^{+62.0}_{-23.2}$	$0.74^{+4.03}_{-2.17}$	90.4/69	0.29	0.62	12.0	25.6	

Table 2—Continued

ID	Total counts and estimated background counts	N_{H} (10^{22} cm^{-2})	Γ	χ^2/dof or c-stat/dof	L_{X} ($10^{44} \text{ erg s}^{-1}$)	$L_{\text{X,in}}$ ($10^{44} \text{ erg s}^{-1}$)	$L_{\text{X}}/L_{[\text{O III}]}$	$L_{\text{X,in}}/L_{[\text{O III}]}$	Compton- thick
(1)	(2)	(3)	(4)	(5)	(6)	(7)	(8)	(9)	(10)
0939+3553	782(136.9)/536(94.3)/544(97.4)	< 0.01	$0.67^{+0.11}_{-0.11}$	192.9/88	0.18	0.18	8.4	8.4	
0945+0355	.../40(31.8)/34(25.5)	< 0.55	1.7	62.8/65	0.002	0.002	0.96	0.96	
1003+5541	141(120.7)/103(91.7)/107(94.4)	< 1.55	$0.80^{+2.02}_{-1.33}$	277.8/321	0.04	0.04	0.54	0.54	
1022+1929	21(4.5)	$1.06^{+2.18}_{-0.84}$	$1.50^{+1.40}_{-1.38}$	25.0/17	0.11	0.12	2.1	2.3	
1034+6001	560(49.8)/124(9.3)/123(12.4)	< 0.03	$2.43^{+0.41}_{-0.17}$	116.2/71	0.005	0.005	0.23	0.23	✓
1034+3939	859(280.9)/307(113.6)/299(120.8)	< 0.03	$2.82^{+0.31}_{-0.17}$	182.5/134	0.005	0.005	0.16	0.16	✓
1039+6430	11(4.3)	< 0.32	1.7	12.2/10	0.02	0.02	1.7	1.7	✓
1044+0637	263(133.9)/100(42.2)/110(52.3)	$68.1^{+29.8}_{-21.8}$	$1.33^{+2.34}_{-1.93}$	62.0/42	0.069	0.49	12.4	88.1	
1106+0357	26(3.6)	< 0.20	$0.81^{+0.58}_{-0.53}$	16.3/20	0.046	0.046	1.2	1.2	✓
1119+6004	1301(1010.9)/326(215.8)/266(167.0)	< 0.02	$1.99^{+0.34}_{-0.31}$	129.9/90	0.10	0.10	13.3	13.3	
1131+3106	.../38(42.1)/54(49.9)	< 1.44	$2.56^{+4.88}_{-1.54}$	64.2/87	0.03	0.03	2.0	2.0	✓
1145+0241	146(100.0)/.../...	< 0.05	$3.12^{+1.30}_{-1.22}$	153.7/127	0.004	0.004	0.71	0.71	✓
1153+0326	91(2.8)	$0.08^{+0.43}_{-0.08}$	$0.73^{+0.42}_{-0.33}$	87.5/74	1.30	1.30	7.7	7.7	
1218+4706	90(38.8)/144(41.6)/170(50.5)	< 0.04	$2.36^{+0.42}_{-0.36}$	34.5/33	0.004	0.004	0.3	0.3	✓
1226+0131	221(27.4)/186(32.6)/216(50.0)	$2.42^{+0.70}_{-0.61}$	$1.69^{+0.30}_{-0.24}$	96.9/93	3.24	3.93	13.4	16.2	
1227+1248	221(141.9)/62(26.2)/50/(37.0)	< 0.15	1.7	323.5/305	0.009	0.009	0.75	0.75	✓
	66(0)	$20.6^{+11.7}_{-8.3}$	$1.86^{+1.02}_{-1.13}$	58.2/59	0.07	0.18	5.8	15	
	27(2.0)	$26.6^{+35.7}_{-19.1}$	$2.33^{+2.34}_{-2.27}$	20.0/23	0.04	0.13	3.3	10.8	
	22(0)	$6.66^{+9.44}_{-3.85}$	1.7	16.4/20	0.03	0.04	2.5	3.3	
		$19.9^{+10.5}_{-8.6}$	$1.78^{+0.96}_{-0.96}$	98.0/103					
1228+0050	54(3.3)	$13.2^{+12.1}_{-8.9}$	$1.55^{+0.67}_{-1.38}$	51.3/45	1.17	2.21	15.8	30.6	
1232+0206	12(2.8)	$7.45^{+13.8}_{-5.52}$	$2.11^{+2.01}_{-1.62}$	17.8/13	0.09	0.33	0.14	0.87	✓
1238+0927	1616(150.3)/540(57.2)/545(53.4)	$45.3^{+6.5}_{-4.7}$	$2.26^{+0.29}_{-0.23}$	313.0/246	0.18	1.00	14.5	80.6	
1243-0232	11(0.6)	$0.41^{+15.0}_{-0.41}$	1.7	12.8/8	0.007	0.008	0.16	1.17	✓
1301-0058	50(4.0)	$11.1^{+8.4}_{-5.9}$	$2.16^{+1.59}_{-1.40}$	74.1/42	0.18	0.39	3.5	7.8	✓
1311+2728	385(125.5)/102(33.3)/101(33.4)	< 0.11	$2.48^{+0.58}_{-0.20}$	416.7/434	0.015	0.015	1.4	1.4	✓
	19(0)	$0.21^{+0.66}_{-0.21}$	$2.55^{+2.35}_{-1.24}$	5.6/13	0.01	0.01	0.9	0.9	
1324+0537	61(42.8)/20(15.3)/50(29.2)	< 0.12	$1.69^{+1.68}_{-0.86}$	128.1/123	0.02	0.02	16.7	16.7	✓
1329+1140	344(254.9)/131(111.6)/140(123.8)	$0.25^{+0.52}_{-0.25}$	$2.73^{+1.47}_{-0.94}$	426.9/472	0.13	0.14	1.5	1.6	
1337-0128	.../.../12(5.0)	< 2.02	1.7	19.6/10	0.065	0.065	3.3	3.3	
1347+1217	1110(5.6)	$2.74^{+0.26}_{-0.25}$	$1.59^{+0.26}_{-0.25}$	600.7/383	0.32	0.40	18.7	23.2	
1411+5212	6159(43.1)	$19.52^{+1.59}_{-1.37}$	$3.56^{+0.11}_{-0.05}$	416.5/238	2.35	10.22	238	1036	
1430-0056	15(9.5)/6(8.3)/10(6.1)	< 0.23	1.7	38.5/28	0.023	0.023	2.3	2.3	✓

Table 2—Continued

ID	Total counts and estimated background counts	N_{H} (10^{22} cm^{-2})	Γ	χ^2/dof or c-stat/dof	L_{X} ($10^{44} \text{ erg s}^{-1}$)	$L_{\mathrm{X},\text{in}}$ ($10^{44} \text{ erg s}^{-1}$)	$L_{\mathrm{X}}/L_{[\text{O III}]}$	$L_{\mathrm{X},\text{in}}/L_{[\text{O III}]}$	Compton- thick
(1)	(2)	(3)	(4)	(5)	(6)	(7)	(8)	(9)	(10)
1431+3251	124(1.5)	$39.9^{+30.4}_{-16.5}$	$1.85^{+1.71}_{-1.02}$	9.1/9	0.69	3.01	5.4	23.6	
1449+4221	31(0.5)	< 0.24	$-0.33^{+0.82}_{-1.54}$	56.9/35	0.21	0.21	7.7	7.7	
1507+0029	754(492.4)/162(90.7)/161(84.2)	$6.23^{+20.9}_{-5.35}$	$0.54^{+0.42}_{-0.84}$	104.9/102	0.23	0.30	6.3	8.2	
1641+3858	991(68.4)/438(25.0)/450(25.7)	$2.28^{+0.48}_{-0.41}$	$1.34^{+0.14}_{-0.14}$	210.9/174	5.31	6.20	12.6	14.7	
1713+5729	314(241.2)/71(45.2)/82(46.9)	< 0.03	$2.53^{+0.42}_{-0.43}$	75.1/43	0.008	0.008	0.26	0.26	✓
2358–0009	39(34.6)/22(14.9)/14(13.9)	$0.26^{+1.43}_{-0.26}$	$2.27^{+0.48}_{-0.23}$	58.9/72	0.11	0.11	0.45	0.45	✓
	42(27.9)/12(7.4)/15(10.5)	< 0.27	$3.68^{+5.60}_{-1.98}$	55.9/63	0.015	0.015	0.06	0.06	
		< 0.37	$2.24^{+2.32}_{-1.17}$	114.8/136					

Note. — Column 1: ID in *hhmm+ddmm* notation; Column 2: total and background photon counts for each detector; Column 3: fitted column density; Column 4: fitted photon index; Column 5: reduced χ^2 or *C*-statistic; Column 6: observed hard X-ray (2–10 keV in rest frame) luminosity derived from spectral fit; Column 7: intrinsic hard X-ray luminosity after correction for absorption; Column 8: observed X-ray to [O III] luminosity ratio; Column 9: intrinsic X-ray to [O III] luminosity ratio; Column 10: Compton-thick or not.

Table 3. X-ray counts, count rates, 3- σ upper limits of marginally detected AGNs.

ID (1)	observed counts (2)	S_{\max} (3)	count rates (4)	$f_{2-10\text{keV}}$ (5)	$L_{2-10\text{keV}}$ (6)	Compton-thick (7)
0028–0014 ^a	12 (15.2) (M2)	12.3	0.0081	5.3×10^{-13}	1.2×10^{44}	
0120–0055	2 (0.3)	9.7	0.0010	4.1×10^{-14}	3.9×10^{43}	✓
0134+0014	3 (1.3)	10.4	0.0010	2.3×10^{-14}	1.2×10^{43}	✓
0149–0048	1 (1.2)	7.3	0.0007	1.6×10^{-14}	1.3×10^{43}	✓
0319–0058	9 (2.9)	18.0	0.0016	3.5×10^{-14}	3.6×10^{43}	✓
0737+4021	3 (0.2)	11.5	0.0012	2.6×10^{-14}	2.6×10^{43}	✓
0815+4304	2 (0.3)	9.7	0.0012	2.7×10^{-14}	1.8×10^{43}	✓
0842+3625	8 (2.2)	17.3	0.0009	4.4×10^{-14}	3.6×10^{43}	✓
0921+5153	1 (0.7)	7.5	0.0007	1.6×10^{-14}	1.4×10^{43}	✓
1027+0032	6 (2.0)	14.4	0.0015	4.3×10^{-14}	4.3×10^{43}	✓
1151+0049	5 (2.4)	12.5	0.0027	8.0×10^{-14}	7.1×10^{42}	
1157+6003	4 (3.3)	10.4	0.0015	3.5×10^{-14}	2.1×10^{43}	✓
1243+1220	6 (1.9)	14.5	0.0014	3.6×10^{-14}	2.2×10^{43}	✓
1431+3251 ^b	9 (1.0)	32.4	0.0064	2.4×10^{-13}	1.0×10^{44}	✓
1446+0113	10 (3.7)	18.6	0.0019	3.7×10^{-14}	5.2×10^{43}	
1517+0331	8 (4.4)	15.1	0.0015	3.2×10^{-14}	3.1×10^{43}	
1606+2725 ^a	15 (15.2) (M1)	15.1	0.0068	3.6×10^{-13}	2.7×10^{44}	✓
2358–0022	5 (2.2)	12.7	0.0020	4.6×10^{-14}	4.8×10^{43}	✓

^aPhotons are obtained by three detectors on *XMM-Newton* for 0028–0014 and 1606+2725. We choose the lowest flux upper limit among PN/MOS1/MOS2 as the flux limit.

^bThe 99.7% Bayesian confidence interval for the source count is (1.7-20.2), which does not give an upper limit. Here we give the 5- σ upper limit on the source count and the corresponding 2-10 keV flux and luminosity.

Note. — Column 1: ID in *hhmm+ddmm* notation; Column 2: observed total counts and the estimated mean background counts (in bracket); Column 3: upper limit on source counts at 3- σ level; Column 4: count rates; Column 5: flux in 2-10 keV range; Column 6: observed hard X-ray (2-10 keV in rest frame) luminosity; Column 7: Compton-thick or not.

Table 4. Fit parameters of double-absorber power-law models.

ID	$N_{\text{H},1}$ 10^{22} cm^{-2}	Γ	$N_{\text{H},2}$ 10^{22} cm^{-2}	ΔC or $\Delta\chi^2$	F -stat	Probability	L_{X} ($10^{44} \text{ erg s}^{-1}$)	$L_{\text{X},\text{in}}$ ($10^{44} \text{ erg s}^{-1}$)	$L_{\text{X}}/L_{[\text{O III}]}$	$L_{\text{X},\text{in}}/L_{[\text{O III}]}$
(1)	(2)	(3)	(4)	(5)	(6)	(7)	(8)	(9)	(10)	(11)
0123+0044		$1.06^{+0.65}_{-0.69}$	$9.7^{+3.8}_{-3.7}$	10.1	6.060	> 0.9969	1.73	2.66	32.6	50.1
0157-0053		$2.03^{+1.57}_{-1.56}$	$48.5^{+106.5}_{-28.0}$	7.3	6.799	> 0.9941	0.30	1.63	5.0	27.4
0801+4412		$1.08^{+1.28}_{-1.29}$	$40.8^{+38.8}_{-24.9}$	20.9	8.377	> 0.9991	0.93	2.90	5.5	17.2
0834+5534	$0.23^{+0.08}_{-0.09}$	$2.78^{+0.48}_{-0.52}$	$7.05^{+16.8}_{-2.89}$	8.4	4.137	> 0.9812	0.22	0.32	11.6	16.9
0853+1753		$2.42^{+0.44}_{-0.38}$	$55.7^{+14.9}_{-11.7}$	81.0	32.78	1	0.08	0.62	2.5	19.4
0900+2053		$1.83^{+0.25}_{-0.15}$	$37.4^{+7.8}_{-10.4}$	216.7	112.6	1	1.10	3.52	30.0	96.0
		$1.54^{+0.52}_{-0.46}$	$52.9^{+50.1}_{-26.6}$	21.0	22.1	> 0.9995	1.21	4.42	33.0	120.5
	$0.12^{+0.02}_{-0.02}$	$2.30^{+0.09}_{-0.09}$	$80.0^{+33.0}_{-27.5}$	90.3	42.55	1	2.50	9.14	68.2	249.3
		$1.81^{+0.15}_{-0.11}$	$37.3^{+7.9}_{-5.8}$							
0913+4056	$0.08^{+0.14}_{-0.08}$	$2.24^{+0.69}_{-0.53}$	$29.2^{+31.6}_{-13.3}$	21.0	10.74	> 0.9999	1.74	5.07	2.1	6.1
		$1.93^{+0.19}_{-0.17}$	$62.1^{+28.2}_{-19.7}$	98.4	41.6	1	2.30	9.28	2.8	11.2
	$0.09^{+0.03}_{-0.03}$	$1.98^{+0.07}_{-0.13}$	$78.0^{+60.6}_{-51.4}$	10.9	5.06	> 0.9932	9.61	16.0	35.1	58.4
		$1.89^{+0.17}_{-0.12}$	$58.3^{+22.9}_{-13.0}$							
0939+3553		$1.73^{+0.26}_{-0.24}$	$11.4^{+4.6}_{-3.0}$	84.3	34.15	1	0.19	0.32	8.9	14.9
1034+6001 ^a	$0.06^{+0.18}_{-0.06}$	$1.75^{+1.81}_{-1.22}$	$26.3^{+42.1}_{-26.3}$	31.9	8.58	> 0.9999	0.009	0.02	0.39	0.87
1034+3939		$2.89^{+0.25}_{-0.23}$	$77.8^{+52.2}_{-52.6}$	37.4	34.28	1	0.02	0.21	0.5	5.0
1044+0637		$2.54^{+1.72}_{-1.44}$	$87.1^{+50.9}_{-33.9}$	20.0	9.52	> 0.9996	0.07	0.96	12.4	170.1
1153+0326	$0.17^{+0.48}_{-0.17}$	$1.54^{+1.18}_{-1.04}$	$8.9^{+17.0}_{-8.9}$	3.2	1.37	> 0.7385	1.33	1.90	7.9	11.2
1218+4706		$2.55^{+0.39}_{-0.30}$	$80.2^{+55.8}_{-41.0}$	12.7	9.03	> 0.9992	0.006	0.02	0.4	1.7
1226+0131	$3.12^{+1.38}_{-0.93}$	$2.18^{+0.78}_{-0.53}$	$121.0^{+257.0}_{-69.5}$	3.7	1.81	> 0.8299	3.16	13.39	13.1	55.2
1227+1248		$2.26^{+0.84}_{-0.66}$	$76.7^{+81.3}_{-41.4}$	47.4	17.28	1	0.04	0.41	3.2	34.2
1238+0927 ^b		$2.26^{+0.29}_{-0.23}$	$45.3^{+6.3}_{-4.7}$				0.18	1.00	14.5	80.6
1311+2728	$0.08^{+0.15}_{-0.08}$	$3.01^{+0.90}_{-0.62}$	$170.0^{+122.0}_{-87.5}$	22.2	12.16	1	0.03	1.79	2.4	163.7
1347+1217	$0.22^{+0.11}_{-0.10}$	$1.59^{+0.32}_{-0.32}$	$4.43^{+0.94}_{-0.85}$	236	81.97	1	0.35	0.47	17.1	20.6
1411+5212 ^b		$3.56^{+0.11}_{-0.05}$	$19.52^{+1.59}_{-1.37}$				2.35	10.22	238	1036
1431+3251	$2.65^{+7.20}_{-2.65}$	$2.37^{+0.72}_{-1.66}$	56.9^c	1.4	0.82	> 0.5197	0.68	5.71	5.4	45.0
1449+4221		1.7	$17.23^{+15.9}_{-8.0}$	13.7	5.55	> 0.9919	0.17	0.38	6.2	13.9
1507+0029	$6.04^{+9.56}_{-4.79}$	$2.51^{+1.11}_{-1.23}$	$66.8^{+32.7}_{-27.9}$	8.5	4.41	> 0.9854	0.23	2.18	6.3	59.2
1641+3858		$1.50^{+0.15}_{-0.17}$	$3.42^{+0.70}_{-0.74}$	14.1	6.16	> 0.9974	5.39	6.75	12.8	16.0

^aSDSS J1034+6001: The photon index of the two power-law components are not tied together in the spectral fits. The other photon indice is $3.01^{+1.51}_{-0.58}$.

^bSDSS J1238+0927, SDSS J1411+5212: Single-absorber power-law spectral fit is not performed.

^cParameter reached preset boundary during error search.

Note. — Column 1: ID in *hmm+ddmm* notation; Column 2: column density of the first absorber; Column 3: photon index of power-law; Column 4: column density of the second absorber; Column 5: change of χ^2 or *C*- statistic compared with the single power-law model; Column 6: calculated F- statistic of adding an additional power-law component; Column 7: significance of the second power-law component; Column 8: observed hard X-ray (2-10 keV in rest frame) luminosity derived from spectral fit; Column 9: intrinsic hard X- ray luminosity after correction for absorption; Column 10: observed X-ray to [O III] luminosity ratio; Column 11: intrinsic X-ray to [O III] luminosity ratio.

Table 5: Fe K α features of the AGNs with visually-detected iron emission line.

ID	E_{line}^a	EW (eV)	L_{Fe} ($10^{42}\text{ergs s}^{-1}$)	χ^2/dof	$\Delta\chi^2$
0834+5534	$6.75^{+0.14}_{-0.11}$	598^{+425}_{-308}	$1.64^{+1.17}_{-0.84}$	107.9/100	18.3
0900+2053	$6.34^{+0.08}_{-0.07}$	$183^{+81.1}_{-78.5}$	$4.36^{+1.93}_{-1.87}$	73.1/76	15.6
0913+4056	$6.44^{+0.10}_{-0.10}$	457^{+473}_{-289}	$17.6^{+18.2}_{-11.1}$	135.9/139	10.4
0939+3553	$6.47^{+0.08}_{-0.09}$	513^{+163}_{-160}	$1.56^{+0.50}_{-0.49}$	108.6/88	30.8
1034+6001	$6.42^{+0.18}_{-0.06}$	1585^{+897}_{-817}	$0.20^{+0.11}_{-0.10}$	84.3/68	18.2
1034+3939	$6.25^{+0.14}_{-0.18}$	452^{+274}_{-294}	$0.16^{+0.10}_{-0.10}$	145.1/133	7.5
1044+0637	$6.30^{+0.13}_{-0.11}$	419^{+254}_{-248}	$0.75^{+0.45}_{-0.44}$	42.0/40	9.2
1218+4706	$6.38^{+0.19}_{-0.22}$	1656^{+2428}_{-1435}	$0.15^{+0.22}_{-0.13}$	21.8/31	8.1
1238+0927	$6.41^{+0.07}_{-0.07}$	111^{+51}_{-51}	$0.47^{+0.22}_{-0.22}$	313.0/246	13.4
1311+2728	$6.45^{+0.13}_{-0.12}$	527^{+363}_{-363}	$0.36^{+0.25}_{-0.25}$	394.5/432	9.6
1347+1217	$6.42^{+0.07}_{-0.08}$	195^{+148}_{-122}	$0.88^{+0.67}_{-0.55}$	360.7/378	4.0

^aIn rest frame

Table 6. Fe K α features of the AGNs without visually-detected iron emission line.

	ID	$L_X/L_{[\text{O III}]}$	E_{line} (eV)	EW (eV)
$-0.5 < \log L_X/L_{[\text{O III}]} < 0$	0056+0032		0.59	
	0758+3923		0.44	
	0840+3838		0.71	
	0945+0355		0.96	$6.43^{+0.04}_{-0.04}$ 1180^{+964}_{-638}
	1003+5541		0.54	
	1145+0241		0.71	
	2358–0009		0.45	
$0 < \log L_X/L_{[\text{O III}]} < 0.5$	0011+0056		1.7	
	0157–0053		2.2	
	0853+1753		2.5	$6.45^{+0.30}_{-0.33}$ 356^{+636}_{-356}
	0923+0101		1.1	
	1022+1929		2.1	
	1329+1140		1.5	
$0.5 < \log L_X/L_{[\text{O III}]} < 1.0$	0050–0039		4.2	
	0210–1001		6.3	
	0801+4412		5.5	
	0855+3709		8.6	$6.38^{+0.06}_{-0.06}$ 360^{+203}_{-166}
	1153+0326		7.9	
	1301–0058		3.5	
	1507+0029		6.3	
$1.0 < \log L_X/L_{[\text{O III}]} < 1.5$	0812+4018		16.4	
	0924+3028		12.0	
	1119+6004		13.3	
	1226+0131		13.1	$6.40^{+0.05}_{-0.06}$ 148^{+104}_{-73}
	1324+0537		16.7	
	1347+1217		17.1	
	1641+3858		12.8	

Table 7. N_{H} from simulation and spectral fitting of *plcabs*. (in units of 10^{22} cm^{-2})

ID	$N_{\text{H,sim}}$	$N_{\text{H,plcabs}}$	ID	$N_{\text{H,sim}}$	$N_{\text{H,plcabs}}$
0011+0056	164.75	1.17	1034+3939	179.23	106
0028–0014	20.34	506	1039+6430	257.28	0.01
0050–0039	104.3	40.9	1044+0637	23.87	89.6
0056+0032	187.11	63.7	1106+0357	133.78	0.27
0120–0055	84.43	0.75	1119+6004	3.09	0.01
0123+0044	12.56	7.97	1131+3106	101.41	9.94
0134+0014	512.3	0.19	1145+0241	84.27	25.56
0149–0048	> 15.32	< 0.17	1151+0049	70.09	5.05
0157–0053	65.79	0.66	1153+0326	34.68	0.86
0210–1001	12.67	1.47	1157+6003	347.69	15.3
0304+0007	75.76	40.4	1218+4706	691.98	0.01
0319–0058	186.81	276	1226+0131	27.89	3.11
0337+0035	6.26	1.96	1227+1248	92.5	86.9
0737+4021	250.59	3.44	1228+0050	27.86	13.4
0758+3923	77.36	2.33	1232+0206	232.56	8.36
0801+4412	77.42	17.6	1238+0927	34.52	45.4
0812+4019	9.54	1.18	1243+1220	154.97	< 3.28
0815–4304	> 8.84	... ^a	1243–0232	154.97	6.32
0834+5534	7.88	0.11	1301–0058	83.5	11.8
0839+3843	0.17	2.37	1311+2728	100.35	0.01
0840+3838	88.06	0.03	1324+0537	131.21	0.64
0842+3625	539.14	6.58	1329+1140	53.96	0.13
0853+1753	108.44	10.34	1337–0128	1.33	0.52
0855+3709	40.81	5.01	1347+1217	12.33	3.15
0900+2053	0.49	0.13	1411+5212	22.18	8.73
0913+4056	63.84	36	1430–0056	95.51	2.43
0920+4531	93.05	0.14	1431+3251	171.58	9.11
0921+5153	> 25.81	< 0.60	1446+0113	46.31	< 0.13
0923+0101	100.57	7.85	1449+4221	39.13	18.4
0924+3028	60.24	3.31	1507+0029	18.26	10.3
0939+3553	4.75	3.58	1517+0331	0.08	0.04
0945+0355	22.81	3.7	1606+2725	151.47	103.6
1003+5541	3.08	0.38	1641+3858	14.3	1.97
1022+1929	71.49	1.32	1713+5729	272.21	0.33
1027+0032	108.61	0.04	2358–0009	138.59	2.99
1034+6001	497.95	606	2358–0022	286.61	9.66

^aDue to limited photon counts and low S/N, *plcabs* could not adequately fit the spectrum.

Table 8: The means of [O III] and X-ray luminosities and their ratios in $L_{[\text{O III}]}$ bins.

$\log L_{\text{OIII}}$ range (L_{\odot})	$\langle \log L_{\text{OIII}} \rangle$ (L_{\odot})	$\langle L_X \rangle$ ($10^{44}\text{ergs s}^{-1}$)	$\langle L_X/L_{\text{OIII}} \rangle$	$\langle L_{\text{Fe}} \rangle$ ($10^{42}\text{ergs s}^{-1}$)
8.0–8.5	8.35 ± 0.14	0.04 ± 0.03	6.01 ± 6.26	0.23 ± 0.14
8.5–9.0	8.75 ± 0.15	0.30 ± 0.58	13.5 ± 23.1	0.88 ± 1.18
9.0–9.5	9.21 ± 0.13	0.38 ± 0.59	5.73 ± 9.09	1.26 ± 1.12
> 9.5	9.88 ± 0.25	2.04 ± 1.61	6.51 ± 1.64	3.85 ± 3.80

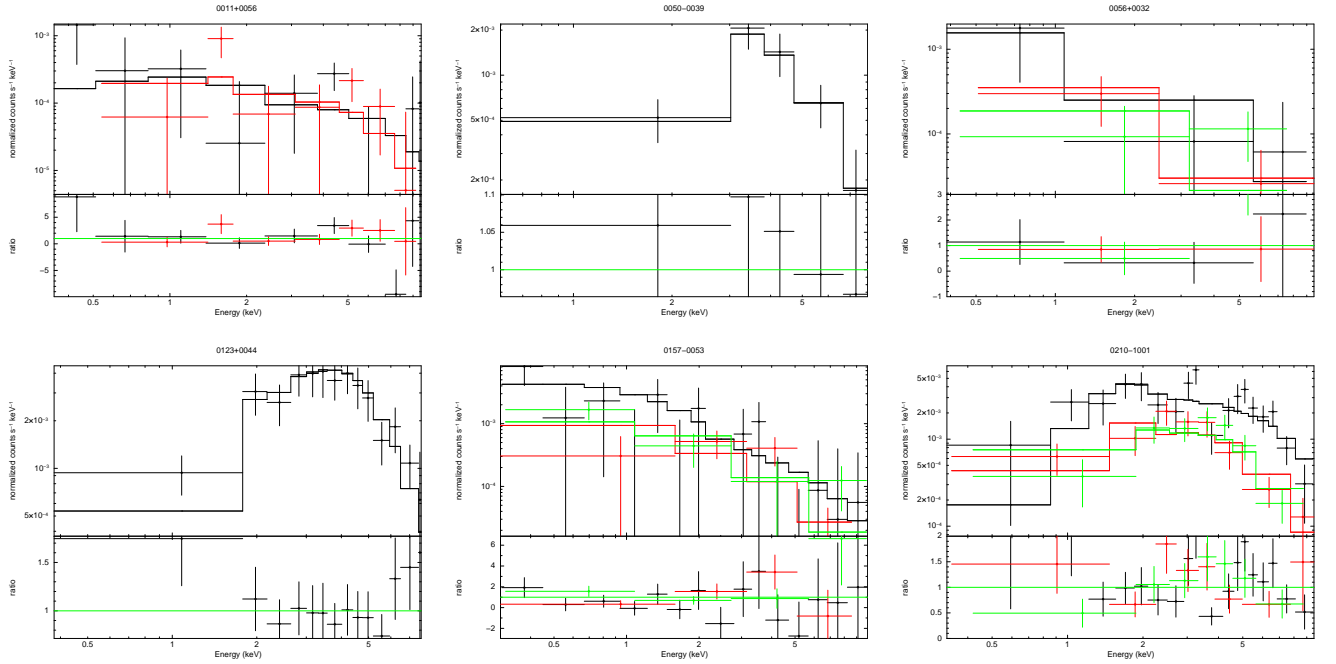


Fig. 1.— Spectra for each target fit with the single-absorber power-law model. The residuals of the fit are shown in the bottom panels. The spectral data in some plots are rebinned for display purpose. (A color version and the complete figure set (52 images) are available in the online journal.)

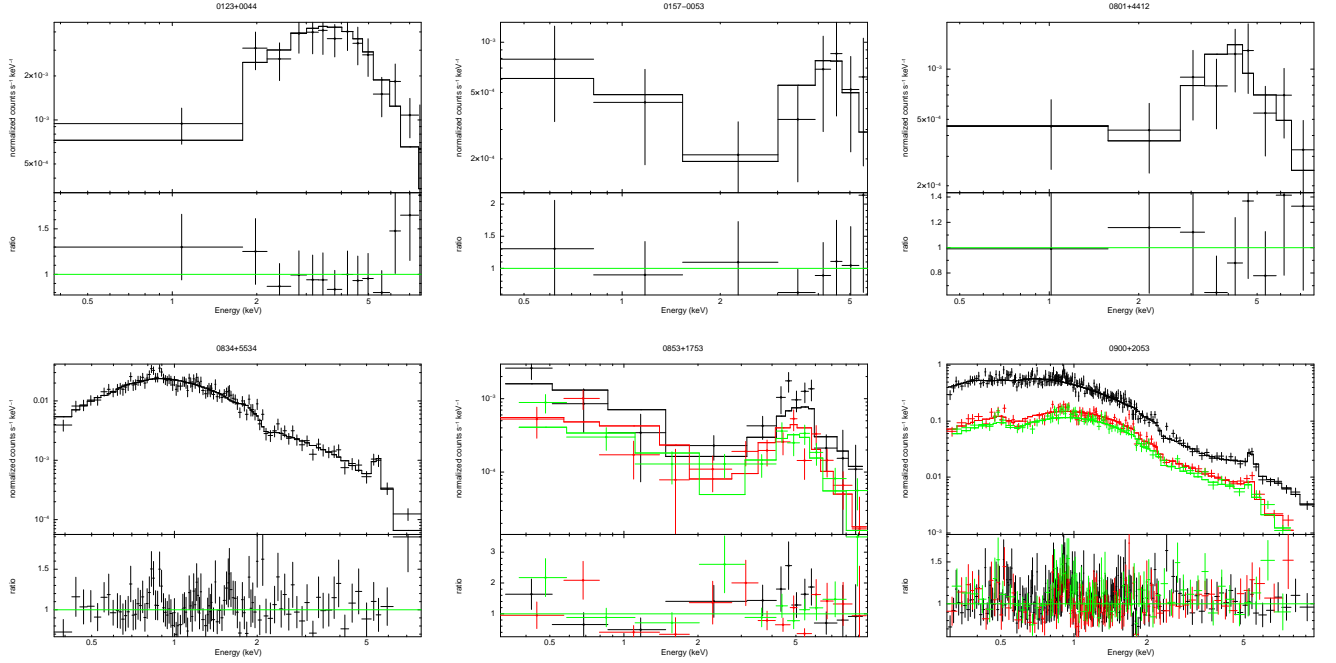


Fig. 2.— Plots of spectral fits using double power-law models. (A color version and the complete figure set (21 images) are available in the online journal.)

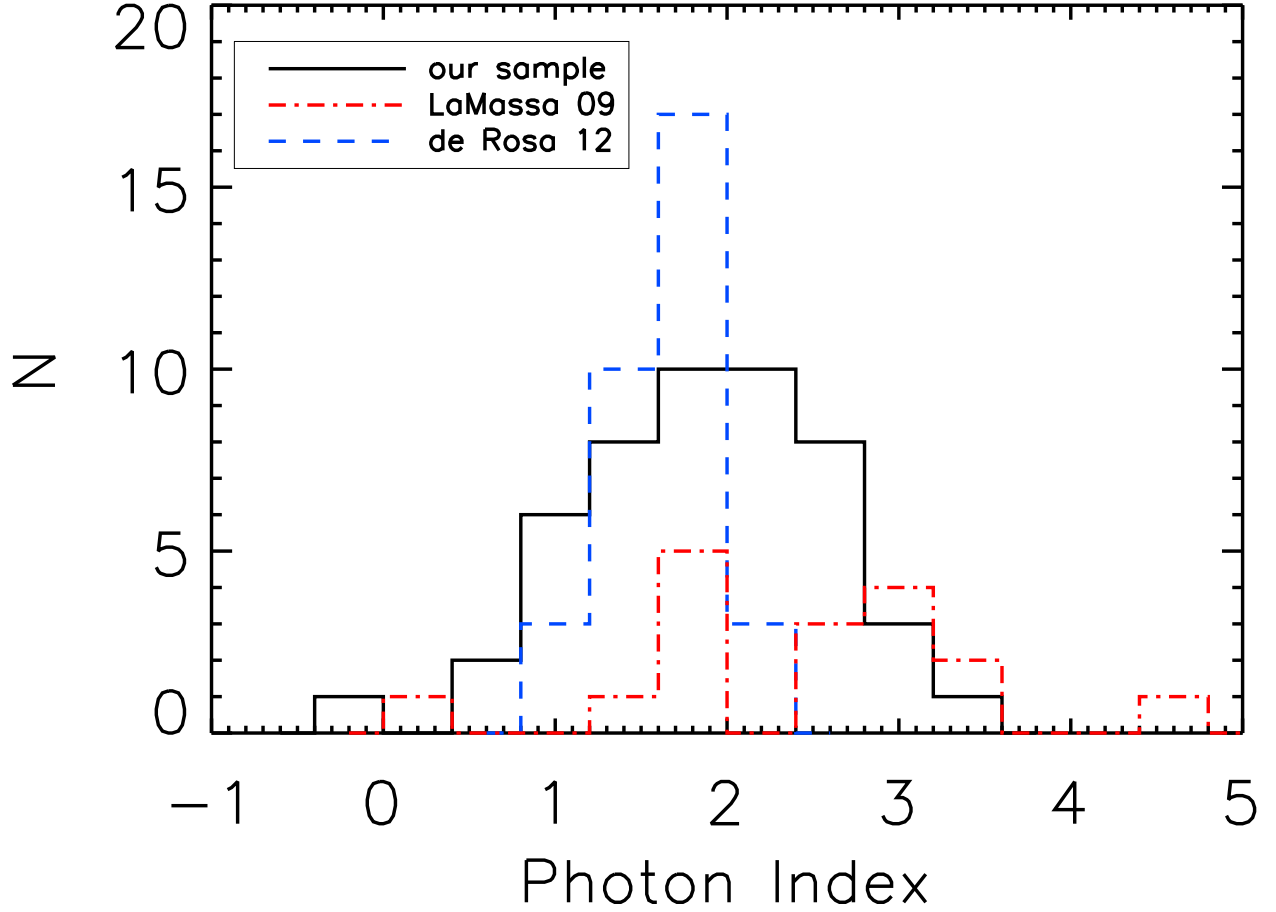


Fig. 3.— Histograms of photon indices of the absorbed power-law spectral fits of our sample (solid black line). For those having spectral fits of both single- and double-absorber power-laws, we use the values derived from the double-absorber model. We also show the sample of hard X-ray selected obscured AGNs (de Rosa et al. 2012, dashed blue line) and the sample of optically selected local Seyfert 2s (LaMassa et al. 2009, dot-dashed red line) for comparison.

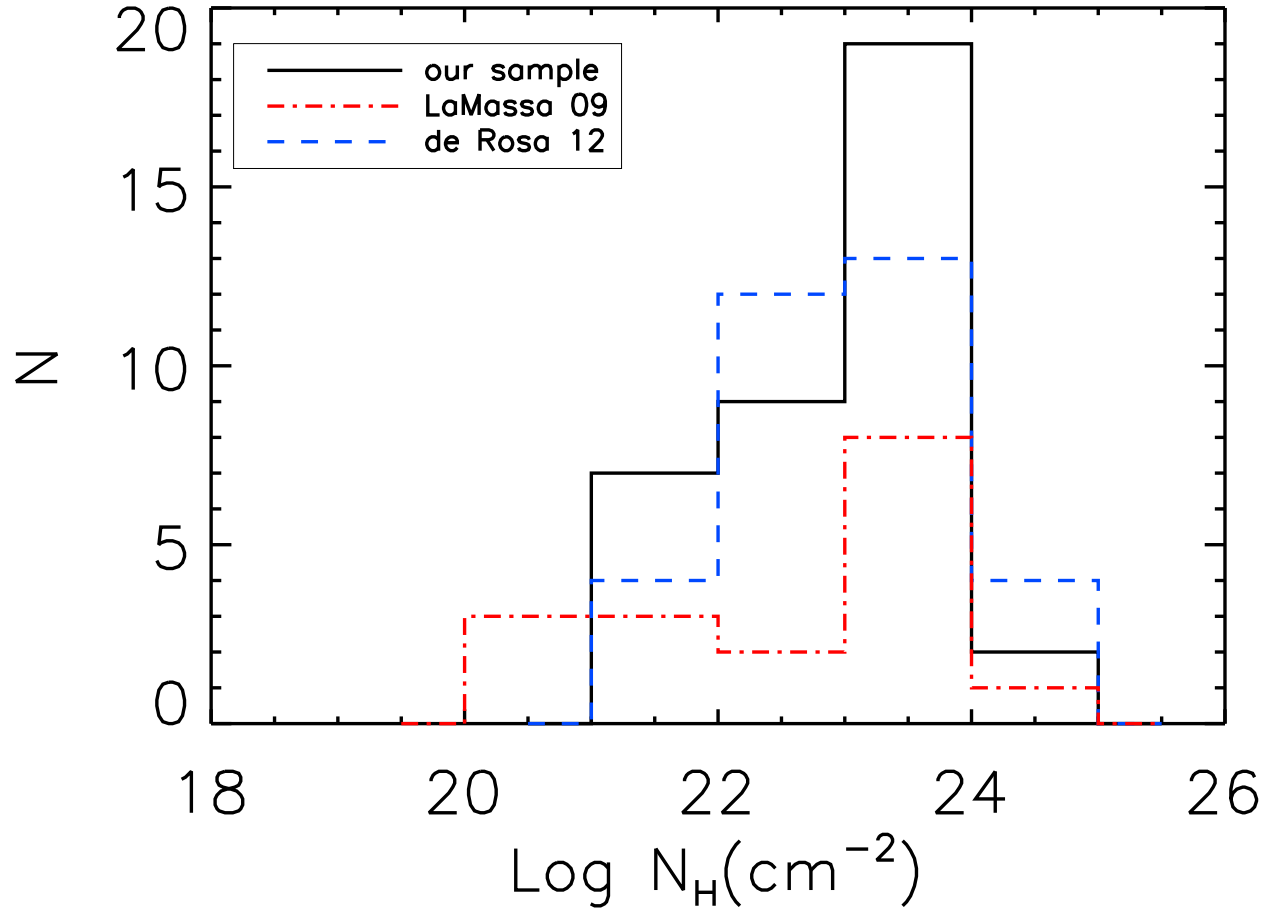


Fig. 4.— Histograms of column densities of the absorbed power-law spectral fits. The samples and line styles are the same as indicated in Figure 3.

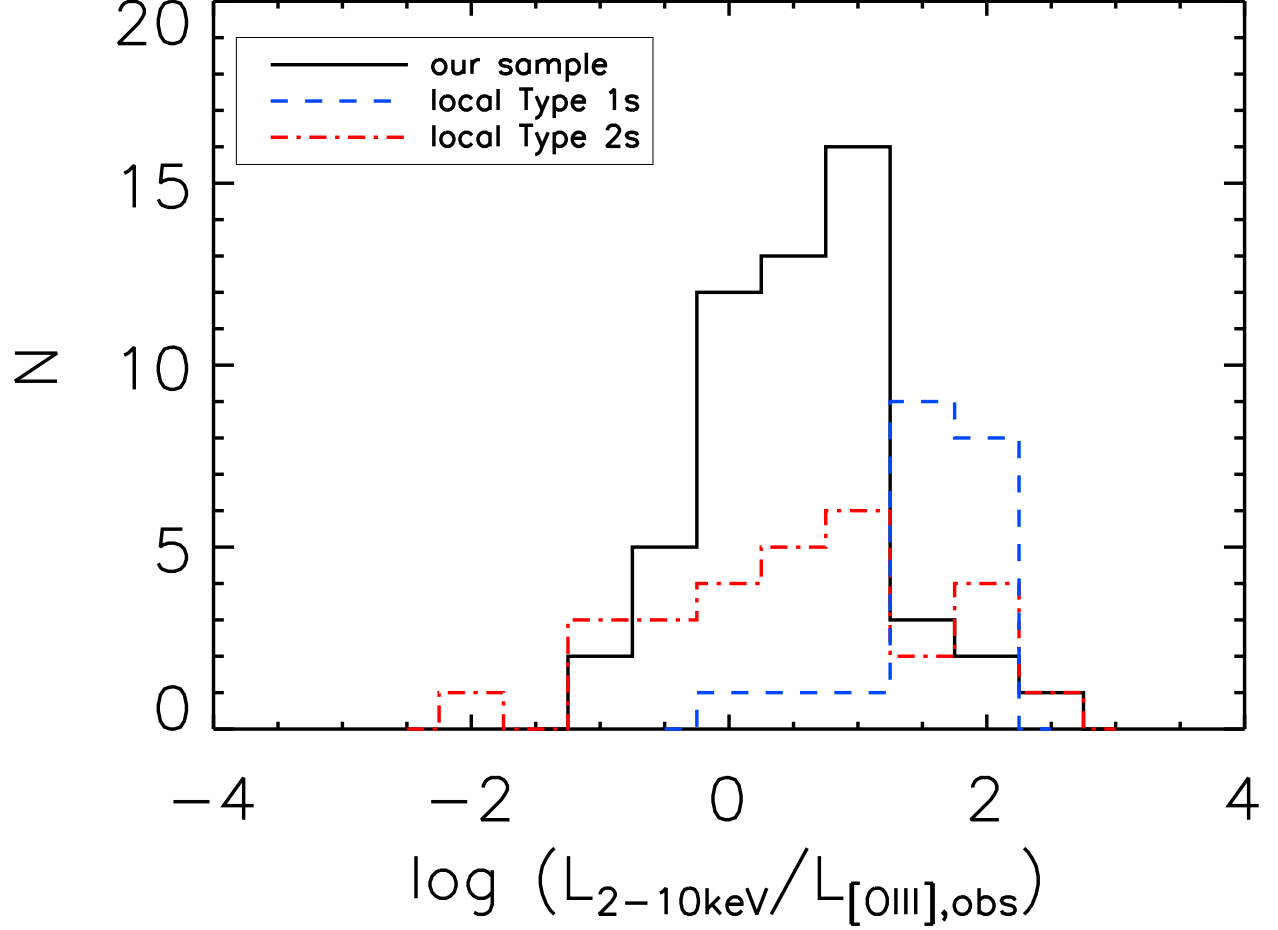


Fig. 5.— Histograms of the ratio of the hard X-ray and observed [O III] λ 5007 emission-line luminosity for local Type 1 (dashed blue line) and Type 2 (dash-dotted red line) of the samples in Heckman et al. (2005) and our type 2 quasar sample (solid black line).

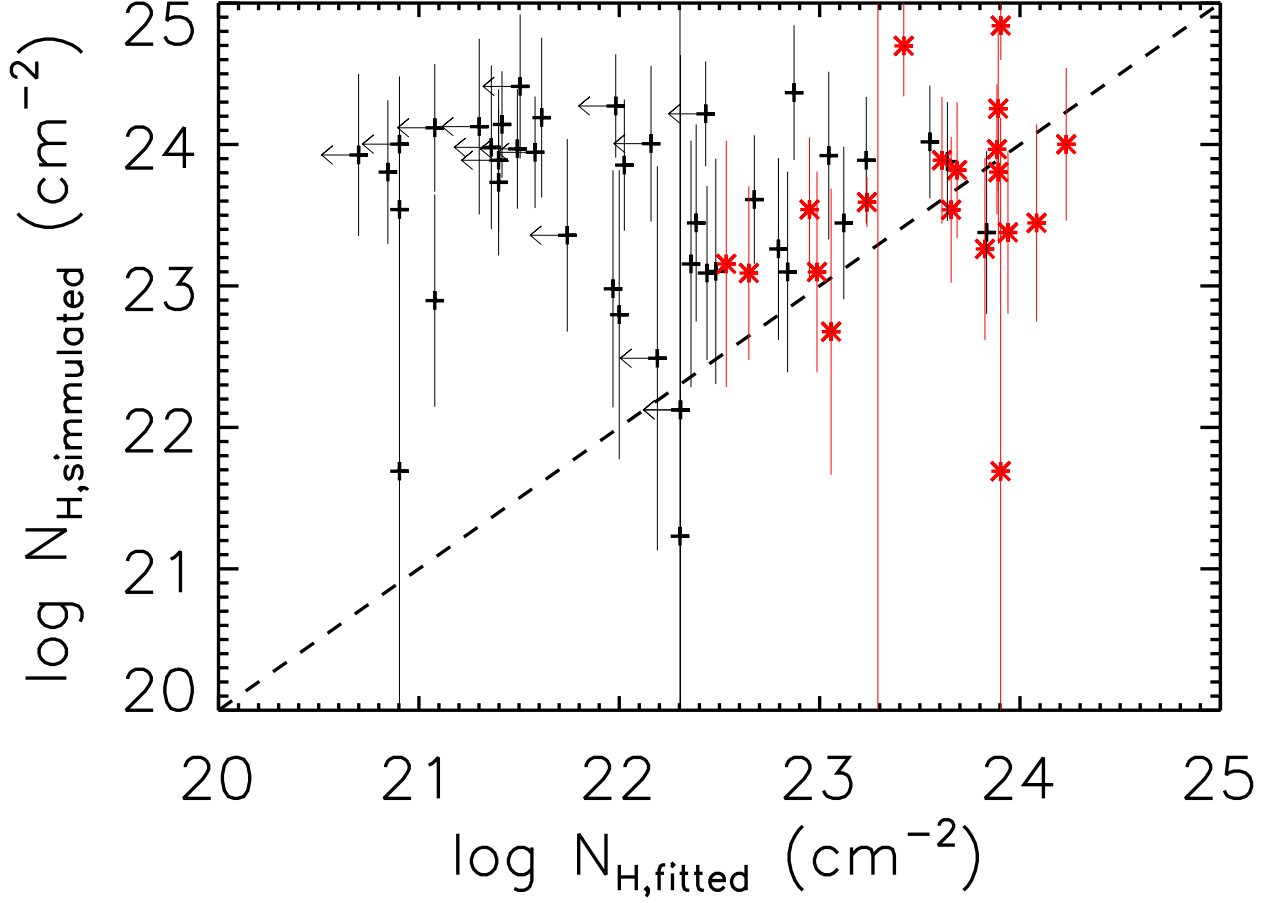


Fig. 6.— Simulated column densities vs. the values from the spectral fits. The dashed line indicates where the two values are equal. The fitted values of column density are from single power-law model (plus symbols in black) and double power-law model (asterisks in red).

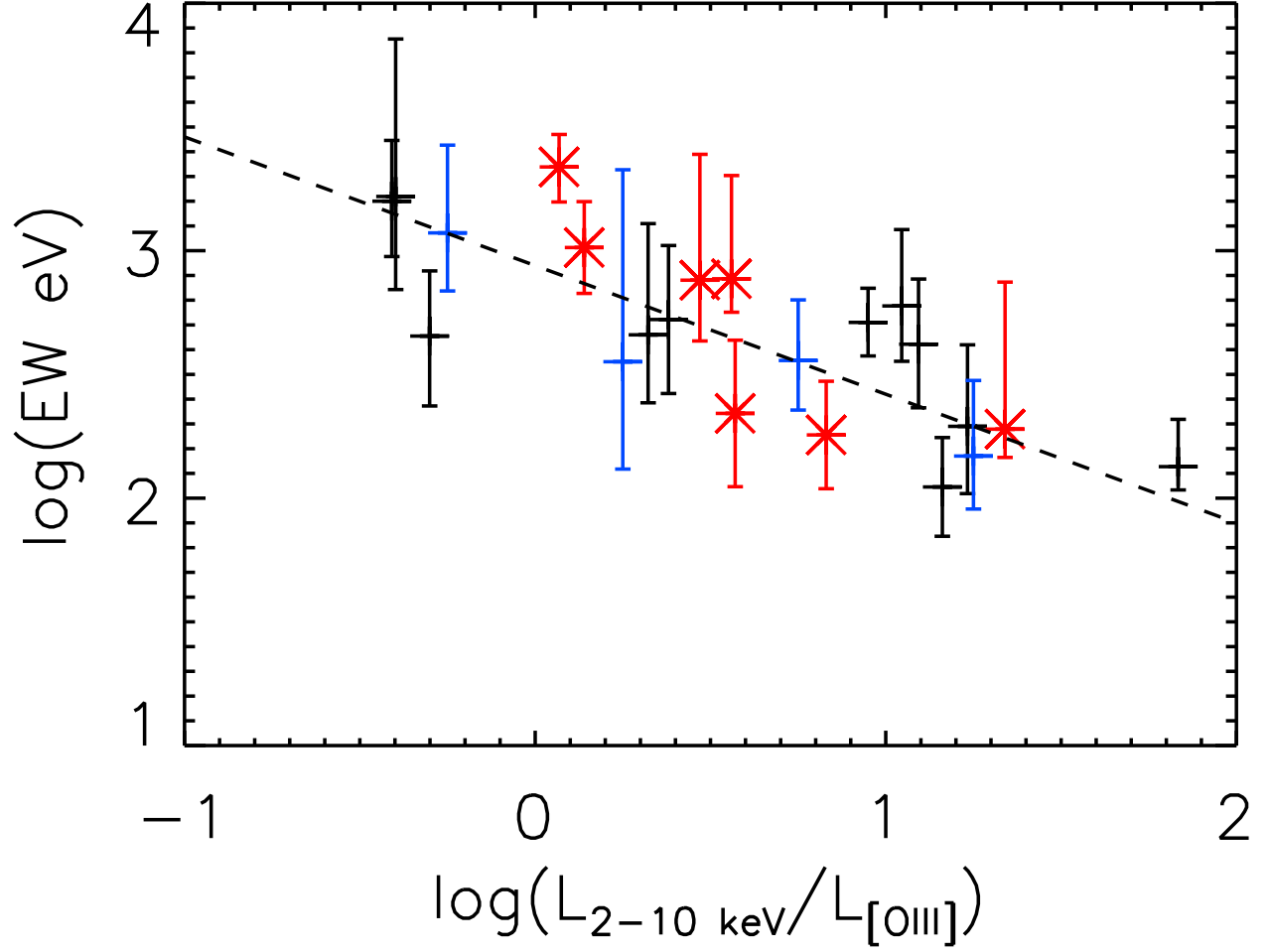


Fig. 7.— Equivalent width of Fe $K\alpha$ emission line vs. $L_{2-10\text{keV}}/L_{[\text{O III}]}$. The data in black and blue are from Table 5 and 6 in our sample, and those in red are from LaMassa et al. (2009).

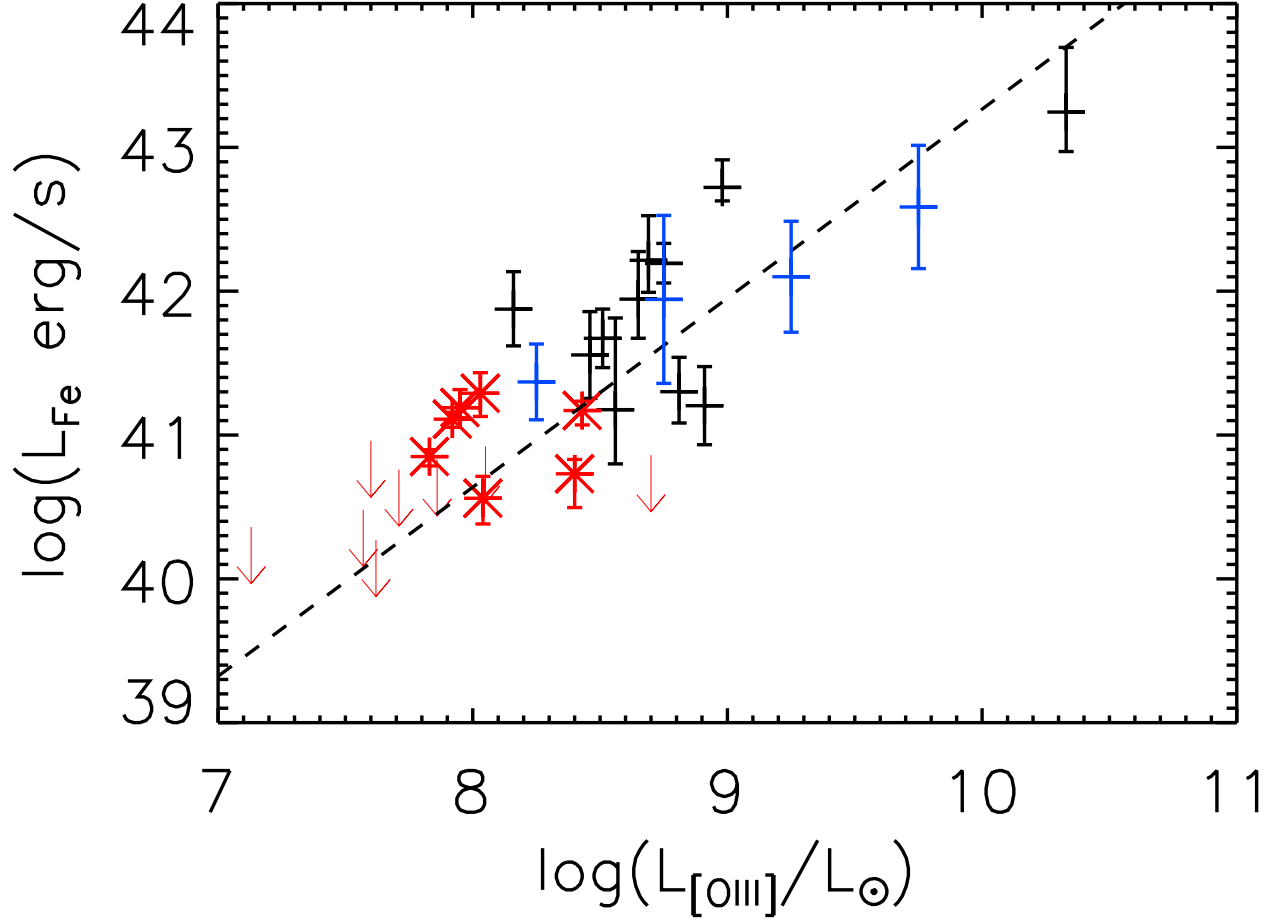


Fig. 8.— Fe K α luminosity vs. [O III] luminosity. The data in red are the sample of type 2 Seyfert galaxies from LaMassa et al. (2009). The black symbols indicate the quasars having iron line detections listed in Table 5, and the blue symbols indicate those from stacking.

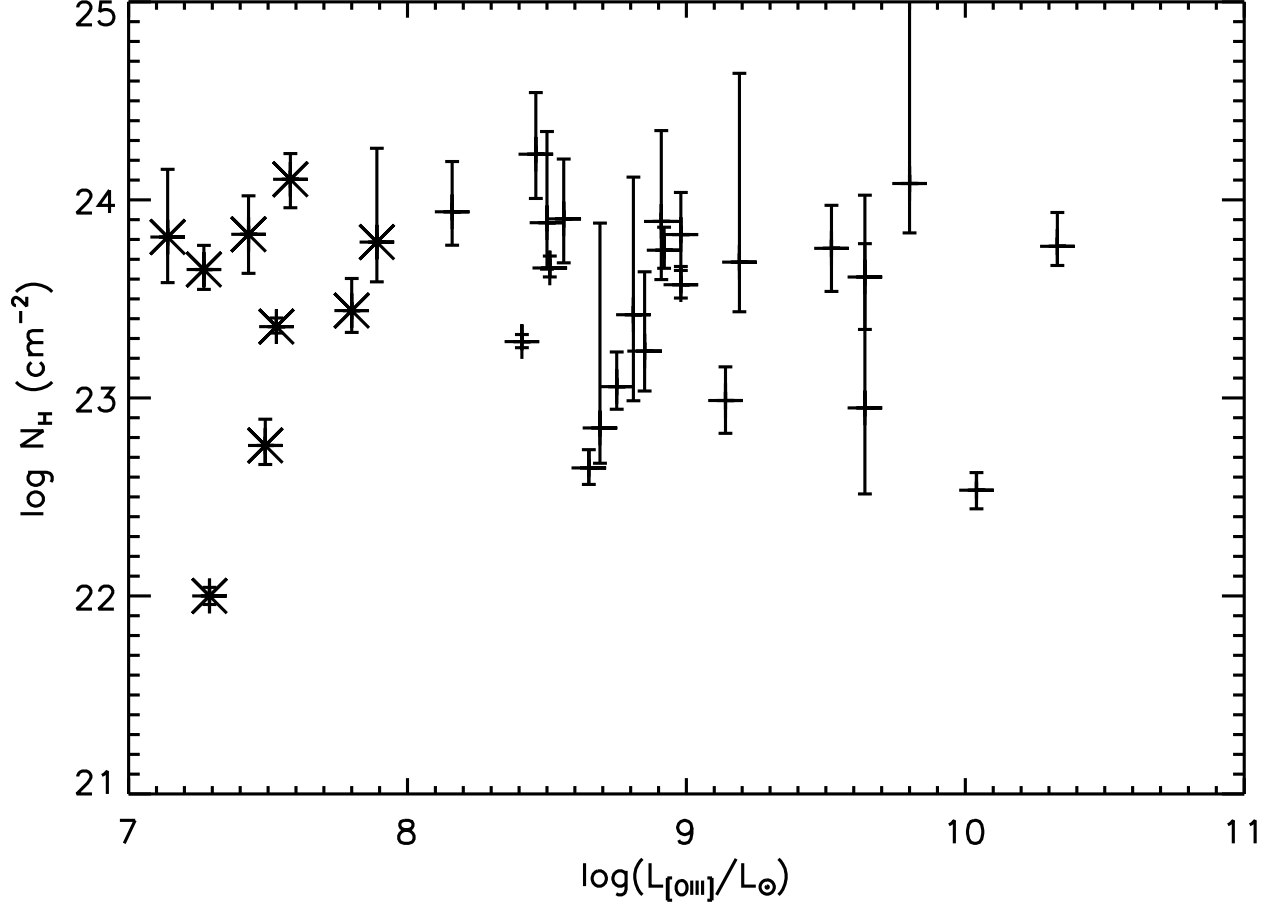


Fig. 9.— Column density of the second absorber ($N_{\text{H},2}$) in Table 4 vs. [O III] luminosity. The crosses are our type 2 quasar sample, while the asterisks are the type 2 Seyferts from LaMassa et al. (2009). There is no correlation between column density and luminosity.

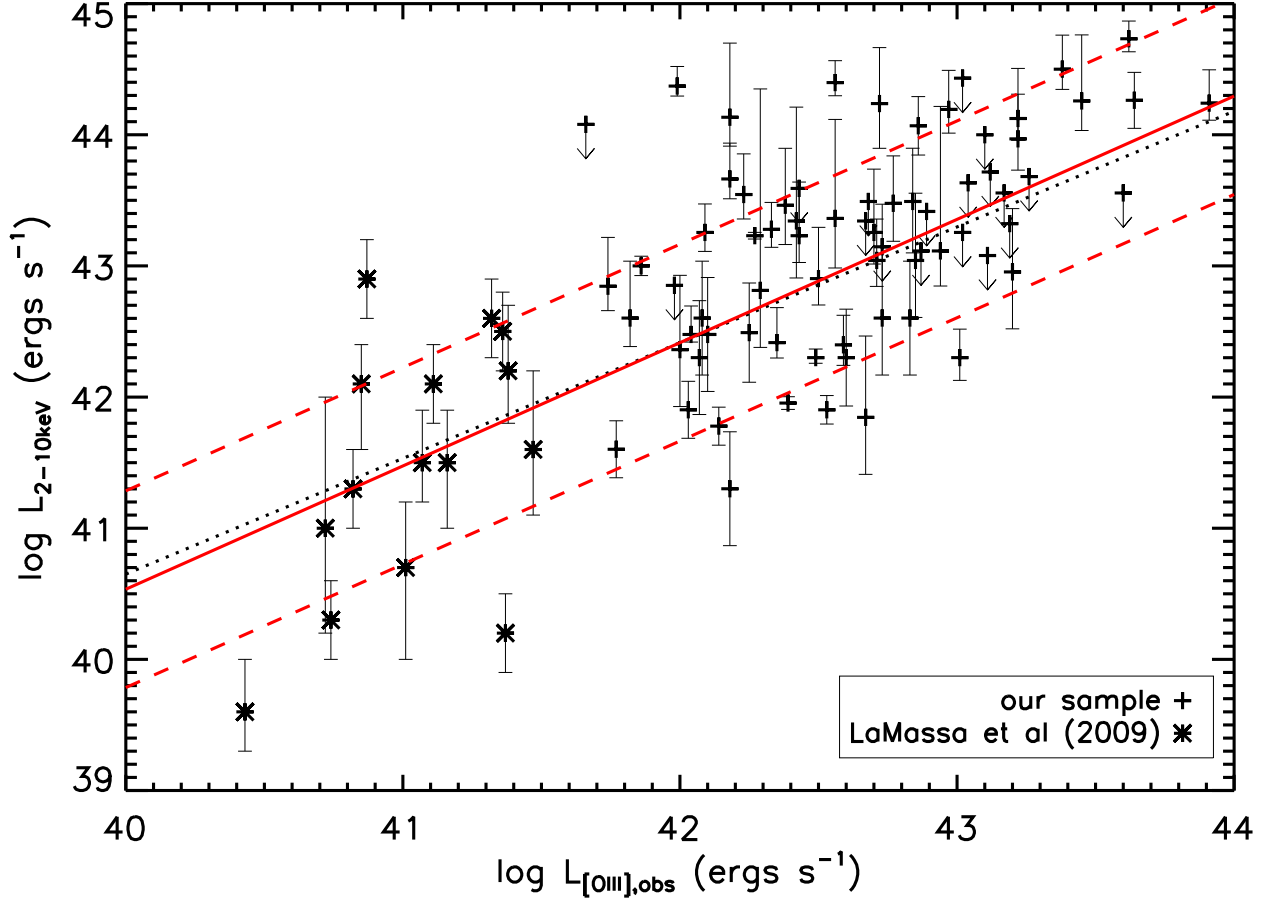


Fig. 10.— The log of the 2-10 keV X-ray luminosity plotted versus the log of the [O III] luminosity. The pluses show our type 2 quasar sample, while the asterisks are the type 2 Seyfert galaxies in LaMassa et al. (2009). The best fit (dotted line) slope (which includes the non-detections in X-rays) is 0.88 ± 0.11 , and is not significantly different from unity. Thus the degree of X-ray obscuration does not depend on AGN luminosity. The solid-red line indicates the best fit slope of the sample of type 1 AGNs given by Jin et al. (2012) with a shift of 1.26 dex downward to line up with the sample in our paper. The dashed-red lines indicate the $\pm 1\sigma$ deviation for the data points in this plot.

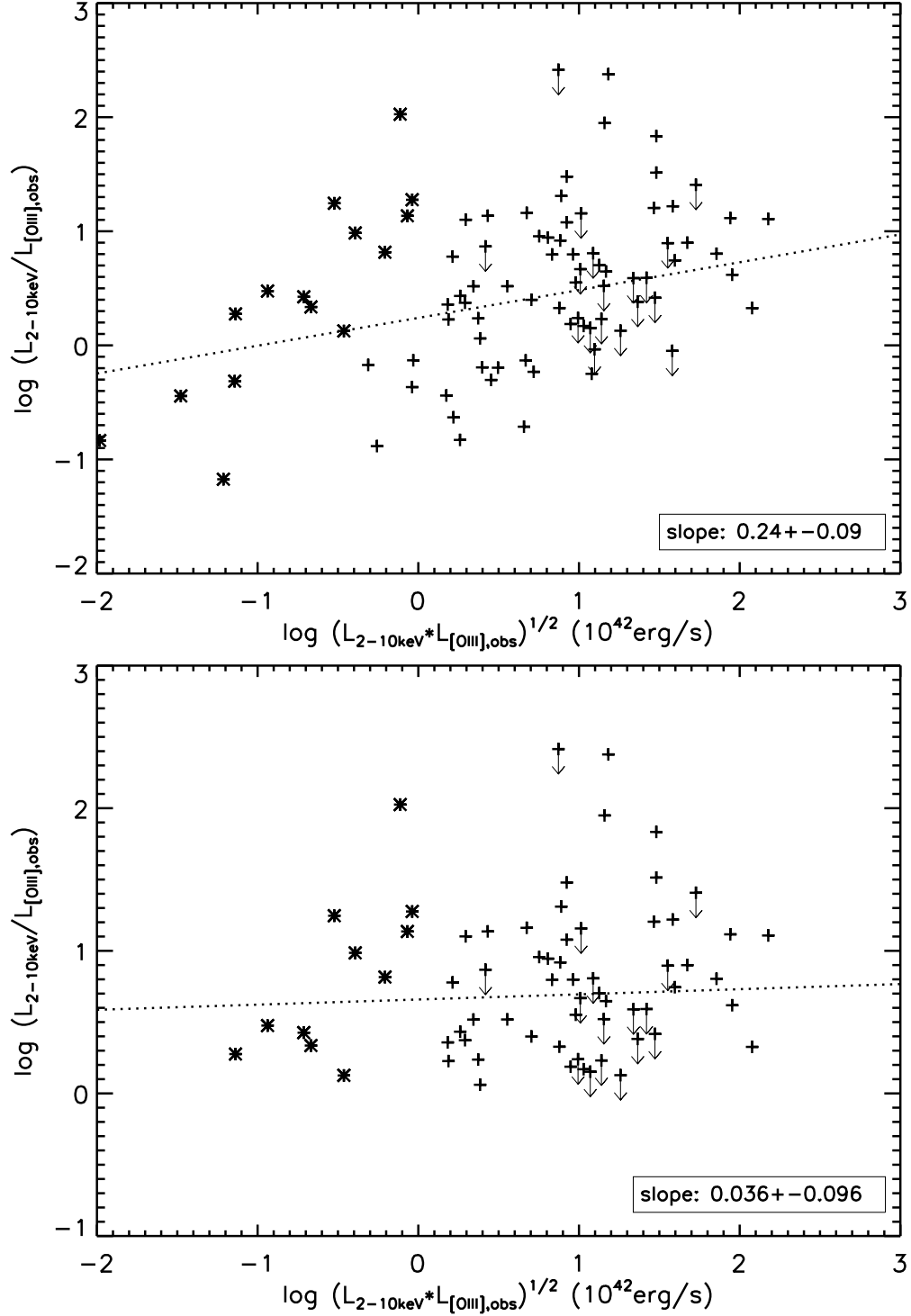


Fig. 11.— $L_X/L_{[\text{O III}]}$ vs. $(L_X \cdot L_{\text{OIII}})^{1/2}$. The upper panel includes all objects from our sample (plus symbols) and LaMassa et al. (2009, asterisk symbols). The lower panel excludes those with $L_X/L_{\text{OIII}} < 1$.

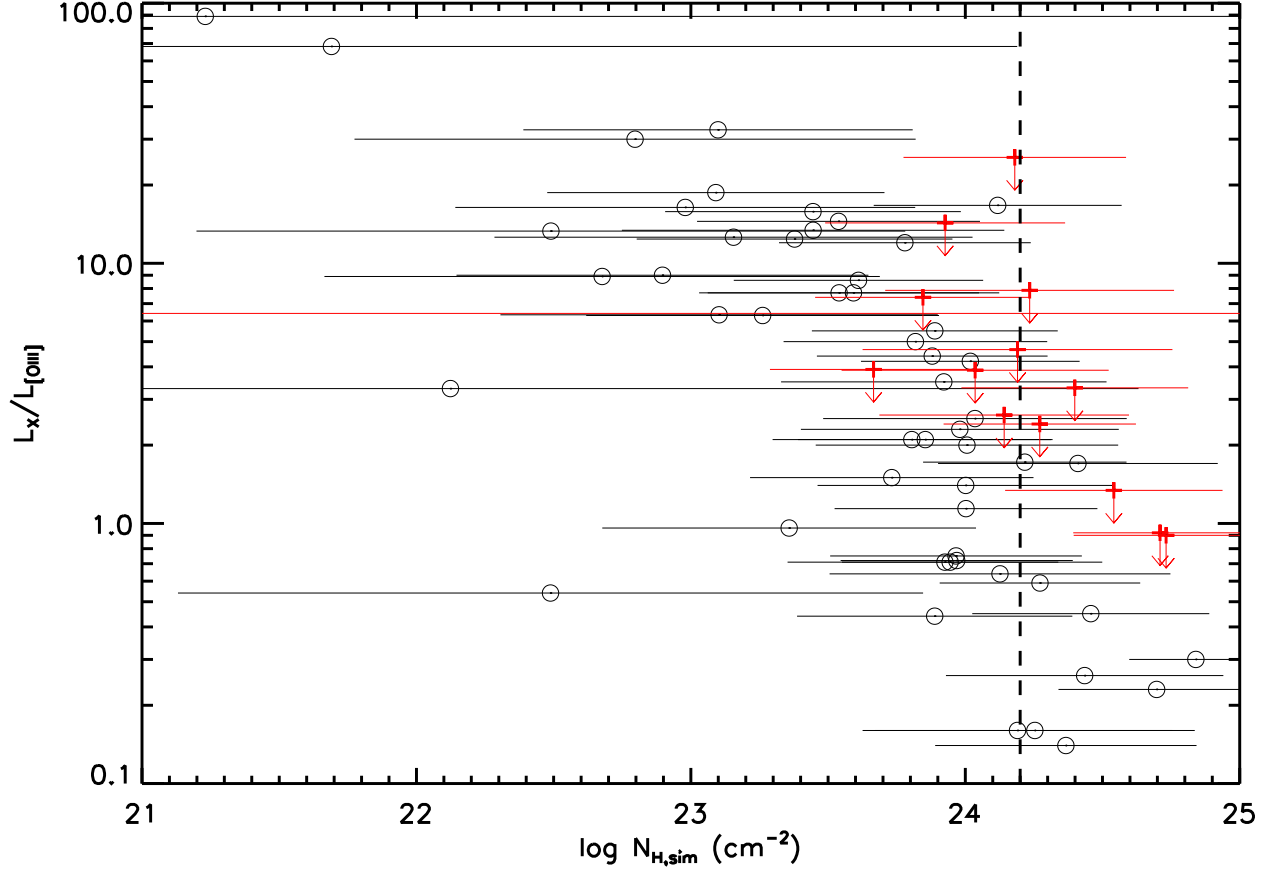


Fig. 12.— Simulated column density vs. observed hard X-ray to [O III] luminosity ratio. The open circles represent the AGNs whose hard X-ray luminosities were derived from their spectral fits listed in Table 2 and 4. The red plus symbols represent upper limit cases in Table 3. The dashed vertical line denotes the region where $N_{H,\text{simulated}} > 1.6 \times 10^{24} \text{ cm}^{-2}$. These objects are designated as Compton-thick AGNs in this work.

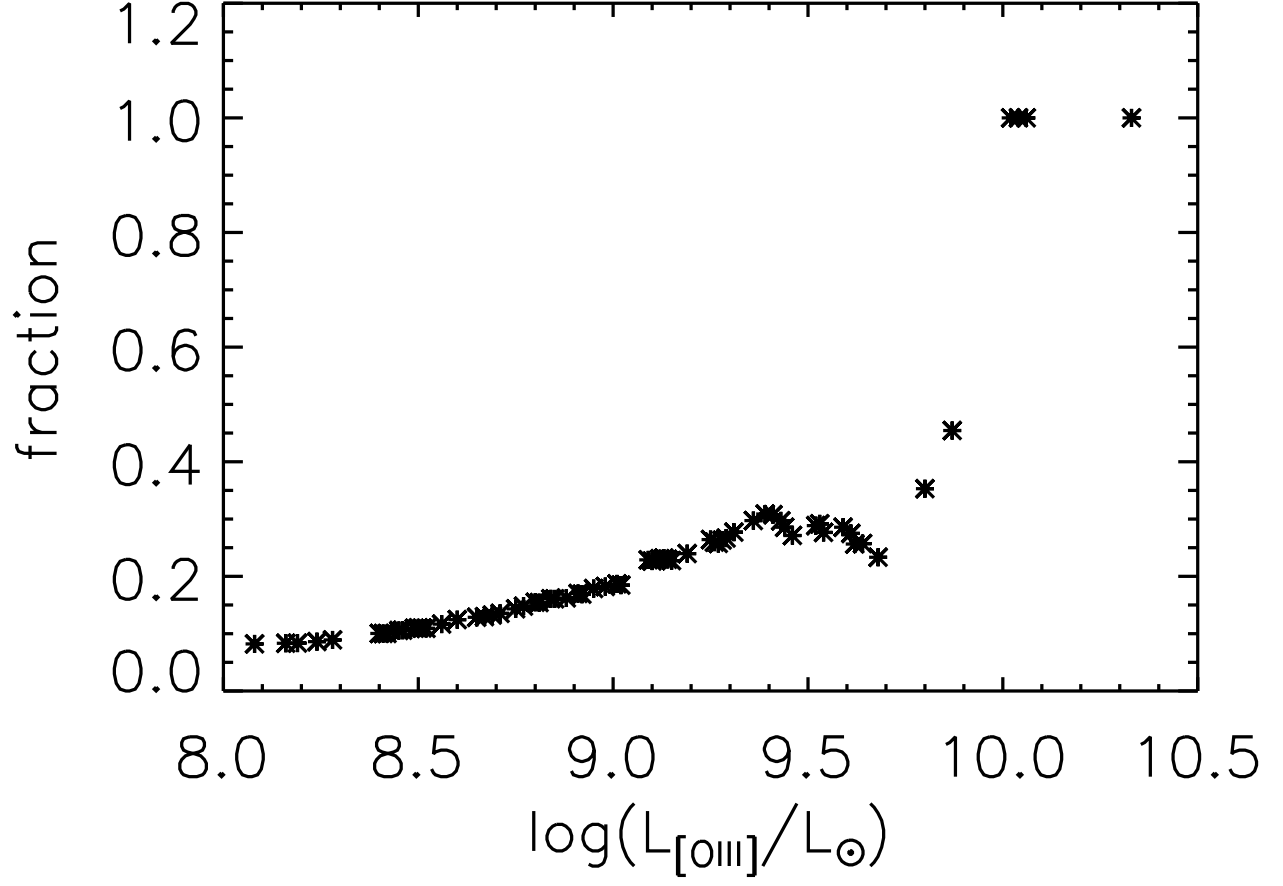


Fig. 13.— The completeness of our sample in the catalog of Reyes et al. (2008) as a function of [O III] luminosity. The fraction is calculated as the number of AGNs in our sample above a given [O III] luminosity (X-axis) divided by the number of all the AGNs in Reyes’ sample above the same [O III] luminosity.

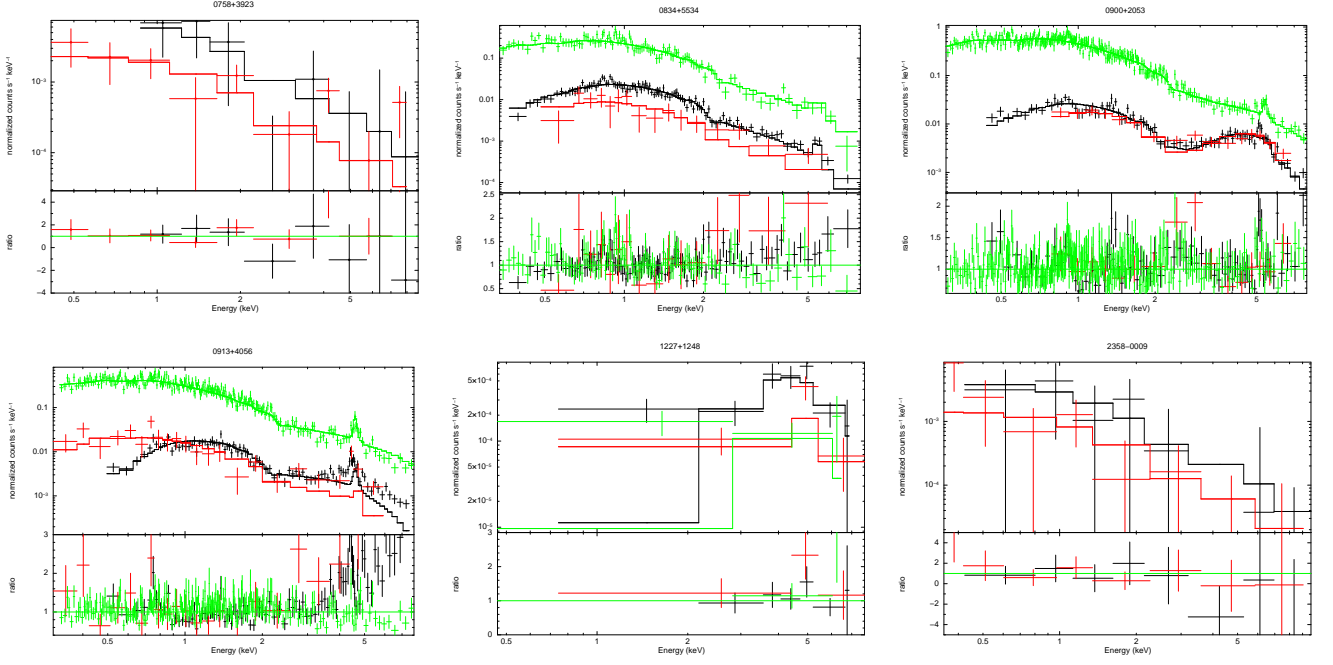


Fig. 14.— *SDSS J0758+3923*: The symbols in black indicate the data obtained by *XMM*-0305990101, and the red symbols are from *XMM*-0406740101. Only PN detections are shown in this plot; *SDSS J0834+5534*: The symbols in black indicate the data obtained by *Chandra*-4940, the red symbols are from *Chandra*-1645, and the green ones are PN data of *XMM*-0143653901; *SDSS J0900+2053*: The symbols in black indicate the data obtained by *Chandra*-10463, the red symbols are from *Chandra*-7897, and PN data of *XMM*-0402250701 are in green color; *SDSS J0913+4056*: The symbols in black and red indicate the data obtained by *Chandra*-10445 and *Chandra*-509, and symbols in green indicate the PN data from *XMM*-0147671001; *SDSS J1227+1248*: The symbols in black, red and green indicate the data obtained by *Chandra*-5912, 9509 and 9510, respectively; *SDSS J2358-0009*: The symbols in black, red indicate the data obtained by *XMM*-0303110301 and 0303110801, respectively.